

MULTIWAVEBAND OBSERVATIONS OF QUASARS WITH FLAT RADIO SPECTRA AND STRONG MILLIMETER-WAVE EMISSION

STEVEN D. BLOOM,^{1,2} ALAN P. MARSCHER, AND E. M. MOORE³
Department of Astronomy, Boston University, 725 Commonwealth Avenue, Boston, MA 02215

WALTER GEAR⁴
Royal Observatory, Blackford Hill, Edinburgh EH9 3HJ, Scotland, UK

HARRI TERÄSRANTA AND ESKO VALTAOJA
Metsähovi Radio Research Station, Metsähovinte 114, FIN-02540 Kylmala, Finland

AND

HUGH D. ALLER AND MARGO F. ALLER
Astronomy Department, University of Michigan, Dennison Building, Ann Arbor, MI 48109

Received 1994 December 27; accepted 1998 December 3

ABSTRACT

We present multiwaveband observations of a well-selected sample of 28 quasars and two radio galaxies with flat radio spectra and strong millimeter-wave emission (referred to here as FSRQs). The data are analyzed to determine the radio to infrared and X-ray to γ -ray properties of FSRQs and the relationships between them. Specifically, the synchrotron self-Compton (SSC) process is examined as a likely common radiation mechanism. For most sources, the broadband spectra are still incomplete, especially in the far-infrared and ultraviolet range. Therefore, precise analysis, such as model fitting of spectra, is not usually possible. To compensate partially for this, we have taken a statistical approach and examine the relationship between high- and low-energy emission by using the data set for the entire sample.

We use very long baseline interferometry (VLBI) at 8.4 and 22 GHz—higher frequencies than those of previous surveys—in conjunction with nearly simultaneous radio to submillimeter-wave observations to determine the parameters of the synchrotron spectrum and to examine the compact angular structure of a subset of sources from our sample. These parameters are used to predict the SSC X-ray flux densities. Seven of 30 sources have predicted self-Compton X-ray flux densities well above the observed flux densities obtained with the *ROSAT* satellite unless one assumes that the radiating plasma experiences bulk relativistic motion directed toward the observer's line of sight. Three of these seven sources are detected at γ -ray frequencies. Model spectra show that the X-rays are consistent with the first-order SSC process, with the simultaneous multiwaveband spectrum of the quasar 0836+710 obtained in 1992 March being very well fitted by SSC emission from a uniform, relativistically moving source. The γ -rays are not produced via second-order self-Compton scattering but rather by either first-order self-Compton scattering or some other process.

A comparison of the *ROSAT* X-ray flux densities and those obtained earlier with the *Einstein Observatory* show that several FSRQs are X-ray variables on timescales of about a decade. Several sources that were observed more than once with *ROSAT* also show variability on timescales of 1–2 yr, with the X-ray variability in these cases often associated with millimeter-wave variability and lower VLBI core-to-jet flux ratios. Detections at γ -ray energies also appear to be related to increases in the radio to millimeter-wave flux densities.

Statistical analysis shows that the millimeter-wave and X-ray luminosities for the sample are strongly correlated, with a linear regression slope ~ 0.65 . The peak in the distribution of X-ray to millimeter spectral indices also indicates a strong connection between millimeter-wave and X-ray emission. Particularly interesting is a correlation between X-ray to millimeter spectral index and fraction of flux density contained in the VLBI core. This tendency toward higher X-ray fluxes from sources with stronger jet emission implies that the knots in the jet are prominent sources of X-rays.

Subject headings: quasars: general — radio continuum: galaxies — X-rays: galaxies

¹ NAS/NRC Resident Research Associate, NASA/Goddard Space Flight Center.

² Current address: Infrared Processing and Analysis Center, Jet Propulsion Laboratory and California Institute of Technology, MS 100-22, Pasadena, CA 91125.

³ Current address: Sterling Software, MS 210-2, NASA Ames Research Center, Moffet Field, CA 94035-1000.

⁴ Current address: Mullard Space Science Laboratory, Holmbury St. Mary, Nr Dorking, Surrey RH5 6NT, United Kingdom.

1. INTRODUCTION

It is clear that in quasars there is a strong relationship between the nonthermal emission at low frequencies and that at high frequencies. Quasars are generally strong X-ray emitters (see, e.g., Tananbaum et al. 1979; Ku, Helfand, & Lucy 1980), and a number have been found to be strong,

hard (>100 MeV) γ -ray sources (Fichtel et al. 1994; Thompson et al. 1995, 1996). Quasars with flat radio spectra—which indicate compact, milliarcsecond-scale structure—and strong millimeter-wave emission (here abbreviated as FSRQs) have been demonstrated to be more luminous in soft X-rays (for a given optical luminosity) than either their radio-quiet counterparts or radio sources with the same radio luminosity but steeper radio spectral index (Owen, Helfand, & Spangler 1981; Zamorani et al. 1981; Ledden & O’Dell 1985; Kembhavi, Feigelson, & Singh 1986; Worrall et al. 1987). Browne & Murphy (1987) have also shown that for a given radio luminosity in extended (arcseconds or greater) structure, the X-ray luminosity tends to be more than an order of magnitude larger for sources with higher compact radio luminosity. Furthermore, except for the Large Magellanic Cloud, bright extragalactic hard γ -ray sources are all FSRQs (or BL Lac objects, which have similar radio–infrared spectra).

These strong correlations between radio and high-energy emission are readily explained if the nonthermal emission at all wave bands is produced via synchrotron self-Compton (SSC) scattering, as has been suggested by many authors (e.g., Jones, O’Dell, & Stein 1974a). This is, however, not the only possibility, since other radiative processes are likely to operate in an environment that produces the highly relativistic electrons and strong magnetic field required for SSC emission (see, e.g., Dermer 1993).

If the SSC process dominates the nonthermal emission, one would expect a correlation between X-ray and γ -ray fluxes and VLBI “core” fluxes. However, a statistical study of the (nonsimultaneous) VLBI core emission and X-ray emission from compact radio loud quasars and active galaxies (Bloom & Marscher 1991) did not conclusively demonstrate a strong correlation, though Zhou et al. (1997) do find a strong relationship between high-energy γ -ray fluxes and VLBI fluxes. Nevertheless, detailed studies of individual sources, both with VLBI and X-ray data, show that the SSC process is a plausible explanation for the X-ray emission (Marscher 1988; Unwin et al. 1994, 1997; Eckart et al. 1986, 1987). The results of these investigations have motivated us to conduct a more detailed study of FSRQs and the relationship between the radio–infrared and the high-energy radiation. The present study not only explores the statistical relationships between high- and low-energy emission but also compares theoretical SSC spectra to multiwaveband data from a set of contemporaneous measurements. Observations over a large range in frequency allow for more accurate determinations of spectral index, spectral peak frequency and flux density, and consequently a more accurate prediction of the Compton flux densities.

This study, which includes high-frequency (8.4 and 22 GHz) VLBI imaging, as well as radio through γ -ray (not all wave bands for all sources) flux density measurements, constitutes the most comprehensive set to date of multiwaveband observations of bright FSRQs. Below we summarize the observations and data analysis. We present our own VLBI, X-ray, submillimeter-wave (submm), and near-infrared (IR) data. A more extensive presentation of previous radio–IR observations used in this work is given by Bloom et al. (1994). We follow with explanations of the procedure for spectral deconvolution and determination of spectral peak frequency and peak flux density, SSC calculations for specific sources, and comparisons of model spectra against the data. In the final sections we present a

statistical analysis of the sample and a general discussion of the results.

2. OBSERVATIONS AND DATA ANALYSIS

2.1. Source Selection

The sample is taken from an essentially complete list of radio sources stronger than 1 Jy at 5 GHz, with spectral indices between 1.5 and 4.9 GHz flatter than $\alpha = 0.5$ ($F_\nu \propto \nu^{-\alpha}$) (Steppe et al. 1988). Quasars and galaxies with 90 GHz flux densities exceeding 0.5 Jy, declinations $\geq 0^\circ$, and measured redshifts exceeding 0.03 were selected from Table III of Steppe et al. (1988) to generate a preliminary sample. This resulted in a sample that had a preponderance of sources with redshifts between 0.4 and 2.25. In order to pare the sample down to a more reasonable size, within the redshift range of 0.4–2.25, only sources with declinations $\geq 30^\circ$ were included in the final sample. BL Lac objects, which form a class distinct from quasars with respect to their soft X-ray emission (Worrall & Wilkes 1990), are excluded, as are optically unidentified objects. The final sample contains 30 sources—28 quasars and two radio galaxies—and is well distributed in redshift. (One source that would have been in the final sample, 3C 216, was dropped from the study owing to its proximity to the Sun during the time of the submillimeter observations.) Because of telescope time allocation limitations, it was not possible to observe the entire sample at all wavelengths. Approximately one-half of this sample was observed from radio to X-ray wavelengths. This subsample was essentially determined by which sources were observed (in priority order) with *ROSAT* prior to the shutdown of the PSPC detector. This might then have caused a selection of objects that were a priori deemed to be more interesting than others. Both radio galaxies, 3C 111 and 3C 120, are included in the subsample. The list of sources, along with a summary of the observations at all wave bands, is presented in Table 1.

2.2. VLBI Data

A subsample of sources has been observed with VLBI at frequencies of 8.4 and 22 GHz. For this work, seven observing sessions were conducted with either the Global VLBI Network or the Very Long Baseline Array⁵ (VLBA; after 1994). The stations of each array (defined by the epoch of the observations) are listed in Table 2. Sessions 1–6 used the Mark II VLBI recording system with a 1.8 MHz bandwidth, while sessions 7–9 used the VLBA recording system with 16 and 32 MHz bandwidth, respectively. Owing to the large sample size, we observed in “snapshot” mode with each source typically observed for four to five scans of one-half hr each during the allotted observing time. Typically three to six sources were observed during each VLBI session. These scan times were chosen to optimize u - v coverage. The video tapes from the individual antennas were correlated using the JPL/Caltech Block II correlator for sessions 1–6 and the VLBA correlator for sessions 7–9. All postprocessing was performed at Boston University using the NRAO AIPS, the CalTech VLB software package, and the difference mapping software Difmap. The phase time and frequency derivatives (fringe delay and fringe rate) were

⁵ The VLBA is an instrument of the National Radio Astronomy Observatory, a facility of the National Science Foundation operated under cooperative agreement by Associated Universities, Inc.

TABLE 1
SUMMARY OF OBSERVATIONS

Source (1)	z (2)	VLBI (3)	JCMT (4)	UKIRT (5)	ROSAT (6)	EGRET (7)
0016+731	1.76	1992 Jun 1992 Sep	1991 Aug 1992 Oct	...	1992 Jul ...	1992 Jul/Aug ...
0133+476	0.86	1992 Jun 1992 Sep	1991 Aug 1992 Oct	1992 Aug ...	1992 Aug ...	1991 Nov/Dec ...
0212+735	2.37	1992 Nov 1993 Mar	1991 Aug	1991 Feb ...	1992 Jul/Aug ...
NRAO 140	1.26	1991 Jun 1991 Nov	1991 Aug 1992 Oct	1992 Aug ...	1992 Aug ...	1991 May ...
3C 111	0.05	1991 Jun 1991 Nov	1991 Aug 1992 Oct	...	1991 Mar 1993 Feb	1991 Nov/Dec ...
0429+415	0.41	1992 Jun 1992 Sep	1991 Aug 1992 Oct
3C 120	0.03	1991 Jun 1991 Nov	1991 Aug 1992 Oct	...	1991 Feb ...	1992 Aug ...
0552+398	2.36	1992 Jun 1992 Sep	1991 Aug 1992 Oct	...	1993 Mar ...	1992 June ...
0642+449	3.40	1991 Jun ...	1991 Aug 1992 Jan	...	1991 Mar
0736+017	0.19	1991 Jun ...	1991 Aug 1992 Oct	...	1991 Apr 1992 Apr	1992 Nov ...
0804+499	1.43	1992 Jun 1992 Sep	1991 Aug 1992 Oct	1993 Nov 1994 Mar	1992 Oct ...	1992 Jan ...
0820+560	1.42	...	1991 Aug	1993 Dec	1993 Oct	...
0836+710	2.17	1992 Jun 1992 Sep	1992 Mar 1992 Oct	...	1992 Mar 1992 Nov	1992 Jan 1992 Mar
0917+449	2.18	1995 Jan	1992 Oct/Nov	...
4C 39.25	0.70	...	1991 Aug 1992 Oct	1993 Nov ...	1991 Apr 1991 Apr	1992 Sep/Oct ...
0945+408	1.25	1992 Nov 1993 Mar 1995 Jan	1992 Oct	1994 May 1994 May ...	1993 Nov 1993 Nov ...	1992 Sep/Oct 1993 Sep/Oct ...
0954+556	0.91	...	1992 Oct	1993 Dec	1993 Nov	1991 Jun/Jul
0955+476	1.87	1995 Jan	1992 Oct	1993 Dec	1993 Nov	...
1150+497	0.334	...	1992 Mar 1992 Oct 1995 Jan	1992 Jun	1992 Jun/Jul
1150+812	1.25	...	1992 Mar	...	1992 Apr 1992 May 1992 Oct	1991 Jan
1611+343	1.40	1992 Nov ... 1996 May	1992 Oct	1992 Aug	1992 Sep 1993 Jan ...	1992 Sep
1633+382	1.81	1992 Sep 1993 Mar	1992 Oct ...	1992 Aug ...	1992 Aug ...	1992 Nov 1993 Sep
1638+398	1.66	...	1992 Oct	1992 Sep	1991 Sep	...
1641+399	0.60	1992 Nov 1993 Mar	1992 Oct	1990 Jun 1992 Jan	1991 Sep ...
1828+487	0.69	...	1991 Aug	1991 Sep
1954+513	1.22	1995 Jan	1991 Aug	1991 May/June
2005+403	1.74	1995 Jan	1991 Aug	1991 May/June
2037+511	1.69	...	1991 Aug 1992 Oct 1995 Jan	1991 May/June
2136+141	2.43	1991 Jun 1991 Nov	1991 Aug	1991 May ...	1992 Jan/Feb ...
2201+315	0.30	1995 Jan	1991 Aug	...	1993 Dec	1991 May/June

determined using the global fringe-fitting algorithm FRING in AIPS (Schwab & Cotton 1983). The amplitudes were calibrated in the usual manner as described by Cohen et al. (1975). Inconsistencies in the calibration of flux densities were corrected by using u - v crossing points and then finding the best-fit flux density using a χ^2 test. A hybrid

mapping procedure was used to obtain images of the sources (see, e.g., Pearson & Readhead 1984). Hogböm's CLEAN algorithm was used to deconvolve the dirty beam from the dirty image to determine the true source brightness distribution. A Gaussian restoring beam with dimensions equal to those of the central portion of the dirty beam was

TABLE 2
VLBI ANTENNAS

Observatory	Location	Diameter (m)	Sessions ^a
Onsala Space Observatory	Onsala, Sweden	20	1, 2, 3, 4, 5, 6
Max-Planck-Institut für Radioastronomie.....	Effelsberg, Germany	100	1, 2, 3, 4, 5, 6
Instituto di Radioastronomia	Medicina, Italy	32	1, 2, 3, 4, 5, 6
Instituto di Radioastronomia	Noto, Italy	32	1, 2, 3, 4, 5, 6
Metsähovi Radio Research Station.....	Metsähovi, Finland	14	3, 4
Haystack Observatory	Westford, MA	37	1, 2, 3
Owens Valley Radio Observatory	Big Pine, CA	40	1, 2
National Radio Astronomy Observatory	Green Bank, WV	43	1, 2, 3, 4, 5, 6
National Radio Astronomy Observatory VLBA.....	Hancock, NH	25	5, 6, 7, 8, 9
National Radio Astronomy Observatory VLBA.....	Saint Croix	25	6, 7, 8, 9
National Radio Astronomy Observatory VLBA.....	Socorro, NM	25	1, 2, 3, 4, 5, 6
National Radio Astronomy Observatory VLBA.....	Pie Town, NM	25	1, 2, 3, 4, 5, 6, 7, 8, 9
National Radio Astronomy Observatory VLBA.....	Los Alamos, NM	25	1, 2, 3, 4, 5, 6, 7, 8, 9
National Radio Astronomy Observatory VLBA.....	Fort Davis, TX	25	1, 2, 3, 7, 8, 9
National Radio Astronomy Observatory VLBA.....	Kitt Peak, AZ	25	1, 2, 3, 4, 5, 6, 7, 8, 9
National Radio Astronomy Observatory VLBA.....	North Liberty, IA	25	1, 2, 3, 4, 5, 6, 7, 8, 9
National Radio Astronomy Observatory VLBA.....	Owens Valley, CA	25	3, 4, 5, 6, 7, 8, 9
National Radio Astronomy Observatory VLBA.....	Brewster, WA	25	3, 4, 5, 6, 7, 8, 9
National Radio Astronomy Observatory VLBA.....	Mauna Kea, HI	25	7, 8, 9

^a Session 1:1991.45; Session 2:1991.85; Session 3:1992.45; Session 4:1992.70; Session 5:1992.85; Session 6:1993.18; Session 7:1995.01; Session 8:1995.34; Session 9:1996.34.

convolved with the CLEAN components to produce a final map.

Table 3 summarizes the parameters of the final image for each source at each frequency: elliptical Gaussian restoring beam ($a_{\text{beam}}, b_{\text{beam}}$), the position angle of the beam (θ_{beam} , as measured north through east), the peak flux density per unit beam area, and the contour levels. Table 4 summarizes the Gaussian model parameters used in conjunction with the hybrid mapping procedures, as described above. These are from the model fits to the self-calibrated data. As with the Pearson & Readhead (1988) survey, the limited data only weakly constrain some model components. In Tables 3 and 4, r is the angular distance from the map center, θ_{pos} is the angular position of the component relative to the (arbitrarily placed) origin (measured from north through east), a and b are the FWHM major and minor axes of the assumed elliptical Gaussian brightness distribution of the component, and ϕ is the position angle of the major axis. The uncertainties in the flux densities given are the estimated calibration errors (as opposed to the uncertainty in the model, which is usually larger). Though we have not, in general, estimated the uncertainties for every parameter of each component, we have performed an uncertainty analysis on the angular sizes (characterized as major and minor axes of an elliptical Gaussian here) of some sources. This will be helpful later (§ 3.2) in determining the uncertainty of the predicted Compton flux, which is highly sensitive to the angular size value. In determining the magnitude of the 1σ uncertainties, we use the technique of Biretta et al. (1986). Owing to the large range in the data quality of our snapshot images, there is also a fairly large range in the uncertainties of derived angular sizes. For the four objects observed with the VLBA and also later used for the Compton calculations, the uncertainties are 13% for 0945+408, 0955+476, 1611+343, and 2201+315 respectively; however, for sources observed earlier with the Global VLBI Network, the typical model uncertainties are

several times larger. Figure 1 displays the VLBI images at 8.4 and 22.2 GHz, in order of increasing right ascension for sources mapped with Global VLBI. Figure 2 displays the maps from the VLBA. Note the differences in angular scale, especially between most of the 22 GHz and 8.4 GHz maps.

2.3. Submillimeter and Infrared Data

A detailed description of the data analysis at submillimeter and infrared wave bands is given in Bloom et al. (1994). In Tables 5 and 6 we present data more recently acquired with the JCMT and UKIRT. The last column in Table 5 is a measure of variability amplitude, as determined by the parameter $(F_{\text{max}} - F_{\text{min}})/(F_{\text{max}} + F_{\text{min}})$. The two measured flux densities for this calculation, extracted from the data presented here or in Bloom et al. (1994), are from the two observations that are closest in time. This measurement of the variability amplitude is considered to be significant if there is at least a 2σ separation between the error bars of the highest and lowest point. We have also examined the possibility of variability in the older data (between 1991 and early 1993). The sources found to be variable are discussed in § 2.6.

2.4. X-Ray Data

The Position Sensitive Proportional Counter (PSPC) was used in conjunction with the Woltjer Type I nested mirror system on board *ROSAT* to obtain fluxes over the energy range 0.1–2.5 keV. After initial processing at Goddard Space Flight Center (GSFC), the X-ray data were extracted from tape using the Post Reduction Off-line Software (PROS) routines operating under the NOAO IRAF data analysis package. Before conducting a spectral analysis, the background counts were determined for each source by calculating the number of photons within concentric annuli, centered on the source. The precise sizes of the annuli (typically 2' inner and 3' outer) were determined for each source by displaying the photons per pixel with SAOI-

TABLE 3
VLBI MAP PARAMETERS

Source	Frequency (GHz)	a_{beam} (mas)	b_{beam} (mas)	θ_{beam} (degrees)	Peak (Jy beam ⁻¹)	Contour Levels (% of Peak)
0016+731	8.4	0.54	0.39	5	0.93	1, 2, 3, 5, 10, 25, 75, 90
	22	0.50	0.15	5	0.56	5, 10, 25, 75, 90
0133+476	8.4	1.21	0.38	15	0.52	2, 3, 5, 10, 25, 75, 90
	22	0.70	0.15	7	1.5	5, 10, 25, 50, 75, 90
0212+735	8.4	0.83	0.38	20	1.2	2, 3, 5, 10, 25, 50, 75, 90
	22	0.25	0.18	75	0.50	10, 25, 50, 75, 90
NRAO 140.....	8.4	3.04	0.46	5	1.0	5, 10, 25, 50, 75, 90
	22	0.88	0.18	-5	0.89	5, 10, 25, 50, 75, 90
3C 111.....	8.4	1.33	0.46	8	0.48	2, 3, 5, 10, 25, 50, 75, 90
	22	1.03	0.20	2	1.26	5, 10, 25, 50, 75, 90
0429+415	8.4	1.54	0.39	5	0.40	5, 10, 25, 50, 75, 90
3C 120.....	8.4	4.62	0.46	-10	0.43	5, 10, 25, 50, 75, 90
	22	1.43	0.20	-9	0.41	10, 25, 50, 75, 90
0552+398	8.4	1.39	0.39	-5	4.1	2, 3, 5, 10, 25, 50, 75, 90
	22	0.58	0.18	-5	2.5	3, 5, 10, 25, 50, 75, 90
0642+449	22	0.50	0.20	-14	1.7	3, 5, 10, 25, 50, 75, 90
0736+017	22	1.10	0.20	-10	1.4	10, 25, 50, 75, 90
0804+499	8.4	1.59	0.38	18	0.82	2, 3, 5, 10, 25, 50, 75, 90
	22	0.63	0.15	5	1.36	3, 5, 10, 25, 50, 75, 90
0820+560	22	0.446	0.308	-11.6	0.35	2, 4, 8, 16, 32, 64
0836+710	8.4	0.65	0.45	30	0.95	5, 10, 25, 50, 75, 90
	22	0.33	0.23	-60	1.6	3, 5, 10, 25, 50, 75, 90
0917+449	22	0.533	0.2750	-11.2	1.19	0.5, 1, 2, 4, 8, 16, 32, 64
0945+408	8.4	0.98	0.38	-7	1.49	2, 3, 5, 10, 25, 50, 75, 90
	22	0.49	0.12	-10	0.69	5, 10, 25, 50, 75, 90
	22	0.761	0.332	-27	0.60	2, 4, 8, 16, 32, 64
0955+476	22	0.539	0.273	-12.1	0.93	1, 2, 4, 8, 16, 32, 64
1150+497	22	0.528	0.263	-18.4	1.50	-0.25, 0.25, 0.5, 1, 2, 4, 8, 16, 32, 64
1611+343	22	0.48	0.15	-5	1.28	3, 5, 10, 25, 50, 75, 90
	22	0.696	0.328	-4.4	2.03	4, 8, 16, 32, 64, 90
1633+382	8.4	1.13	0.53	-7	1.153	2, 3, 5, 10, 25, 50, 75, 90
	22	0.61	0.12	-20	0.53	5, 10, 25, 50, 75, 90
3C 345.....	8.4	1.1	0.53	-10	6.768	3, 5, 10, 25, 50, 75, 90
	22	0.75	0.15	-10	4.5	5, 10, 25, 50, 75, 90
1954+513	22	0.629	0.265	12.7	0.69	1, 2, 4, 8, 16, 32, 64
2005+403	22	0.921	0.862	49.9	1.35	1, 2, 4, 8, 16, 32, 64
2037+511	22	0.588	0.266	3.7	1.80	0.5, 1, 2, 4, 8, 16, 32, 64
2136+141	8.4	4.86	0.53	-10	1.75	2, 3, 5, 10, 25, 50, 75, 90
	22	1.5	0.25	-10	1.47	3, 5, 10, 25, 50, 75, 90
2201+315	22	0.626	0.255	-17.4	1.00	0.5, 1, 2, 4, 8, 16, 32, 64

MAGE (see Wilkes 1992). All of the objects in this sample are unresolved with the PSPC, which has a spatial resolution of about 15". Therefore, spatial analysis of the photon counts (i.e., mapping the source) is not possible.

The spectral analysis was conducted using the standard routines within PROS. This consisted of modeling the data in terms of a power-law spectrum over the energy range 0.1–2.5 keV, with absorption at low energies due to intervening gas, parameterized as the column density of hydrogen atoms under the assumption of cosmic abundances. The X-ray photon spectrum is represented by the following equation:

$$\frac{dN}{dE} = KE^{-(\alpha+1)}e^{-N_{\text{H}}\sigma(E)} \text{ photons s}^{-1} \text{ cm}^{-2} \text{ keV}^{-1} . \quad (2.4.1)$$

The predicted spectrum (photon counts per energy bin) using this model was then compared to the observed spectrum using a χ^2 test to determine "goodness of fit." The model parameters that minimize χ^2 were adopted to calcu-

late the total flux over a specified energy band. The default values for the spectral response matrix and effective area of the detector for routines in PROS 2.0 were used to determine the source spectrum from the raw photon spectrum. Some care has to be taken, as χ^2 can be a minimum for parameter values that are physically unrealistic, such as an extremely high column density or a photon index that is much too steep. Uncertainties in model parameters and derived flux values were determined by increasing the value of the parameter by the amount that increases χ^2 to the desired confidence level. Alternatively, in some cases, the normalization parameter, K , of equation (2.4.1) was plotted against spectral index, and the uncertainty in this parameter was taken to be the range of the 68% confidence contour. The flux density was then calculated by using equation (2.4.1) corrected for absorption, and then converting to janskys.

Table 7 summarizes the *ROSAT* X-ray observations. Column (5) is the logarithm of the Galactic hydrogen column density, N_{Hgal} . Unless otherwise noted, this is the value from the Stark et al. (1992) 21 cm emission-line obser-

TABLE 4
VLBI GAUSSIAN MODEL PARAMETERS

Source	Frequency (GHz)	Flux Density (Jy)	r (mas)	θ_{pos} (degrees)	a (mas)	b/a	ϕ (degrees)	A. F. (amplitude)	A. F. (closure phase)
0016+731	8.4	1.61 ± 0.05	0.0	0.0	0.49	0.58	-54.0	3.37	1.03
	22	1.23 ± 0.06	0.0	0.0	0.29	0.60	8.1	1.24	1.21
0133+476	8.4	0.56 ± 0.06	0.0	0.0	0.24	0.50	-4.7	3.13	1.11
		0.14 ± 0.02	1.98	-55.2	1.68	0.56	119.0		
0212+735	22	1.66 ± 0.07	0.0	0.0	0.12	0.14	-0.3	1.28	1.09
	8.4	1.70 ± 0.02	0.0	0.0	0.42	0.52	-42.1	2.08	2.07
NRAO 140.....		0.38 ± 0.01	2.22	102.6	2.58	0.82	-92.6		
	22	1.54 ± 0.06	0.0	0.0	0.32	0.40	-44	1.20	1.31
3C 111.....	8.4	1.16 ± 0.04	0.0	0.0	0.28	0.93	20.6	3.80	1.81
		0.61 ± 0.02	2.03	120	3.64	0.61	5.5		
3C 111.....	22	1.53 ± 0.21	0.0	0.0	0.36	0.65	-8.4	1.98	1.1
		0.19 ± 0.03	1.60	142	2.89	0.53	95		
0429+415	8.4	0.66 ± 0.03	0.0	0.0	0.93	0.38	14.7	1.60	1.19
		0.31 ± 0.01	0.84	66.0	3.48	0.36	61.23		
3C 120.....	22	1.45 ± 0.23	0.0	0.0	0.33	0.72	16.5	1.4	1.2
		0.82 ± 0.12	1.1	61	2.69	0.81	121		
0429+415	8.4	1.05 ± 0.04	0.0	0.0	1.67	0.37	1.8	5.03	2.9
	8.4	0.58 ± 0.04	0.0	0.0	2.1	0.16	-11.1	2.65	1.82
3C 120.....		1.21 ± 0.05	3.16	255.1	3.9	0.73	37.3		
		0.27 ± 0.01	7.03	249.8	4.07	0.38	-15.1		
0552+398	22	0.61 ± 0.21	0.0	0.0	0.35	0.53	12	1.27	1.15
		0.47 ± 0.16	2.5	-109	0.88	1.0	69		
0552+398		0.34 ± 0.11	5.5	-108	1.4	1.0	88		
	8.4	6.95 ± 0.23	0.0	0.0	0.60	0.82	-7.3	3.17	1.59
0642+449	22	5.88 ± 0.34	0.0	0.0	0.30	0.77	-6.0	2.05	1.12
	22	2.55 ± 0.27	0.0	0.0	0.21	0.71	-91.6	1.06	1.27
0736+017	22	1.58 ± 0.47	0.0	0.0	0.07	0.36	29	0.87	1.27
		0.45 ± 0.14	0.52	-78	0.41	0.48	-19		
0804+499		0.16 ± 0.05	2.30	-83	3.15	0.001	48		
	8.4	0.97 ± 0.06	0.0	0.0	0.40	0.60	7.04	1.60	1.11
0820+560		0.09 ± 0.05	1.82	72.0	4.02	0.13	11.0		
	22	1.67 ± 0.25	0.0	0.0	0.27	0.19	16.8	1.00	1.40
0820+560	22	0.44 ± 0.07	0.0	0.00	0.25	0.23	-67.5		
		0.21 ± 0.03	0.78	105.6	2.97	0.13	-42.1		
0836+710	8.4	1.44 ± 0.01	0.0	0.0	0.35	0.46	61.6	2.76	2.28
		0.47 ± 0.01	2.33	210.0	1.65	0.61	14.5		
0917+449	22	1.77 ± 0.13	0.0	0.0	0.18	0.26	32.1	1.64	1.07
	22	1.31 ± 0.07	0.00	0.0	0.20	0.50	7.4	0.27	0.21
0945+408		0.23 ± 0.01	1.13	174.4	0.99	0.48	14.6		
	8.4	1.75 ± 0.25	0.0	0.0	0.27	0.38	-74.6	2.43	1.43
0955+476	22	1.57 ± 0.03	0.0	0.0	0.34	0.59	-20.5	1.05	1.07
		1.09 ± 0.05	0.13	105.0	0.64	0.25	-82.8	0.358	0.304
1150+497	22	1.01 ± 0.05	0.00	0.0	0.12	0.89	79.17	0.742	0.266
	22	1.72 ± 0.09	0.00	0.0	0.19	0.22	19.9	1.132	0.101
1611+343		0.18 ± 0.01	0.61	-155.5	1.32	0.50	31.2		
	22	1.56 ± 0.34	0.0	0.0	0.24	0.38	1.4	4.4	1.33
1633+382		0.26 ± 0.06	0.45	1.68	0.33	0.001	5.3		
	22	1.86 ± 0.09	0.08	106.7	0.22	0.37	-5.7	0.309	0.186
1633+382		0.57 ± 0.03	2.81	171.1	1.61	0.49	-38.7		
		0.57 ± 0.03	0.15	37.1	6.86	0.17	50.0		
3C 345.....	8.4	0.09 ± 0.01	0.86	93.8	1.19	0.10	-21.8		
		1.60 ± 0.04	0.0	0.0	0.52	0.0	84.6	1.29	1.20
3C 345.....		0.41 ± 0.01	0.84	-75.7	0.95	0.89	105.7		
	22	0.79 ± 0.11	0.0	0.0	0.24	0.62	37	1.52	1.29
1954+513		1.18 ± 0.18	2.6	-32	3.16	0.40	-32		
	8.4	9.41 ± 0.09	0.0	0.0	0.50	0.12	87.5	3.56	3.65
2005+403	22	9.26 ± 0.28	0.0	0.0	0.33	0.78	2.9	7.83	1.35
		2.39 ± 0.07	0.29	-87	0.17	0.59	-6.4		
2037+511	22	0.72 ± 0.11	0.00	0.0	0.103	0.10	66.3	0.438	0.190
		0.41 ± 0.06	0.48	-53.5	0.36	0.57	-21.4		
2037+511	22	1.59 ± 0.08	0.0	0.0	0.80	0.14	83.0	0.918	0.498
		0.35 ± 0.02	0.51	75.4	0.83	0.20	60.2		
2037+511	22	1.98 ± 0.10	0.00	0.00	0.18	0.52	-6.5	0.55	0.331
		0.68 ± 0.03	0.75	-157.1	0.88	0.37	83.8		

TABLE 4—Continued

Source	Frequency (GHz)	Flux Density (Jy)	r (mas)	θ_{pos} (degrees)	a (mas)	b/a	ϕ (degrees)	A. F. (amplitude)	A. F. (closure phase)
2136+141.....	8.4	1.70 ± 0.03	0.0	0.0	0.14	0.65	-60.5	4.63	1.23
		0.45 ± 0.01	0.52	-133	1.96	0.94	-24.4		
	22	1.89 ± 0.21	0.0	0.0	0.33	0.5	-23	1.4	1.0
2201+315.....	22	0.49 ± 0.05	0.85	-49	5.7	0.4	-10		
		1.26 ± 0.06	0.0	0.0	0.23	0.25	31.3	0.852	0.457
		0.48 ± 0.02	1.87	-142.9	2.20	0.28	42.2		

vations. However, for two sources, 3C 111 and NRAO 140, we have also added the column density (in atoms cm^{-2}) of molecular hydrogen as inferred from observations of Galactic CO (Bania, Marscher, & Barvainis 1991). Column (6) gives the best-fit value of N_{H} as determined from the χ^2 minimization routine. Column (7) is the best-fit spectral index; if no uncertainties are given, then it is an assumed value. Column (8) is the 1 keV flux density. Columns (9) and (10) give the χ^2 and degrees of freedom (dof, one less than the number of parameters varied subtracted from the total number of energy channels), respectively. When N_{H} is determined from a best fit, then the uncertainties quoted in the

spectral index and flux densities correspond to $\chi^2_{\text{min}} + 3.53$ (68% confidence for three interesting parameters). If N_{H} is assumed to be the Galactic value, then the subsequent uncertainties correspond to $\chi^2_{\text{min}} + 2.3$ (68% confidence for two interesting parameters). If both α and N_{H} are assumed, then the uncertainties are for $\chi^2_{\text{min}} + 1.0$ (68% confidence for one interesting parameter). Generally, the fit is considered reasonable if $\chi^2 \lesssim \text{dof}$. Note that by this criterion two fits are not particularly good (see Table 7). The fit for the first observation of 1150+812 is poor probably because the fit was performed on the combined counts from two scans that were a month apart, each having a low number of individ-

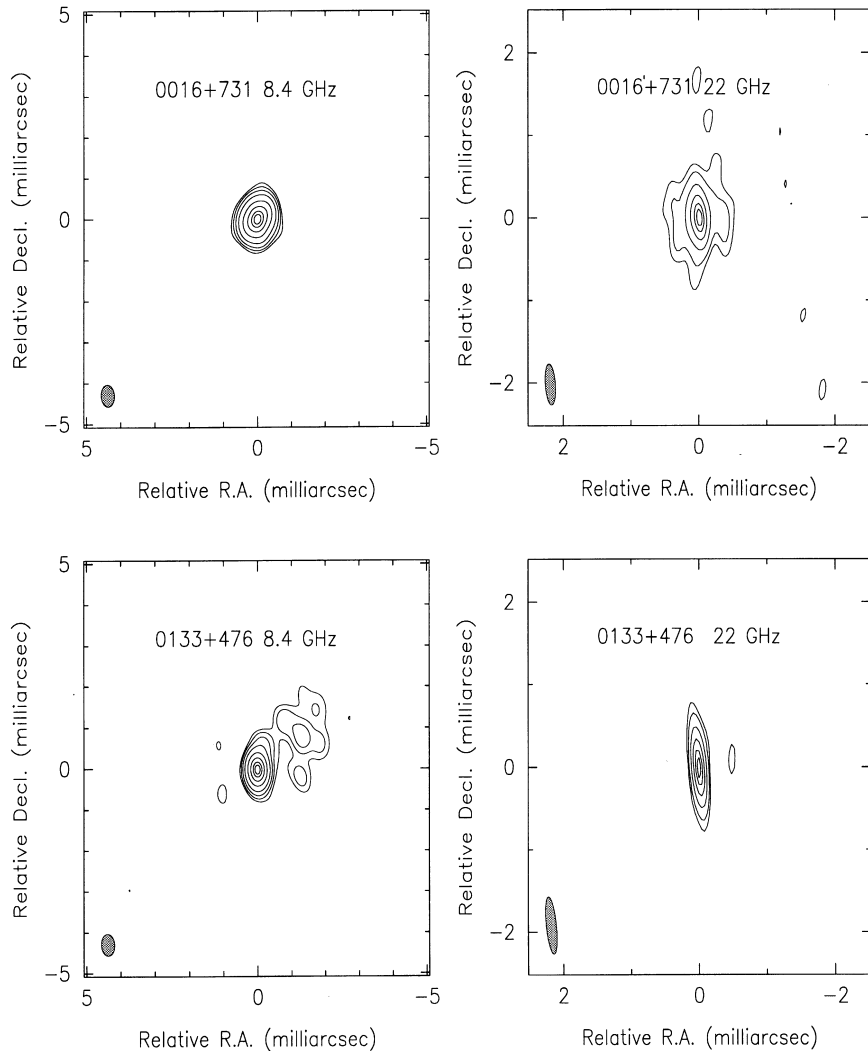


FIG. 1.—VLBI images at 8.4 and 22 GHz from the Global VLBI Network. Parameters of each map are listed in Table 3. The restoring beam is shown in the lower left-hand corner of each separate plot.

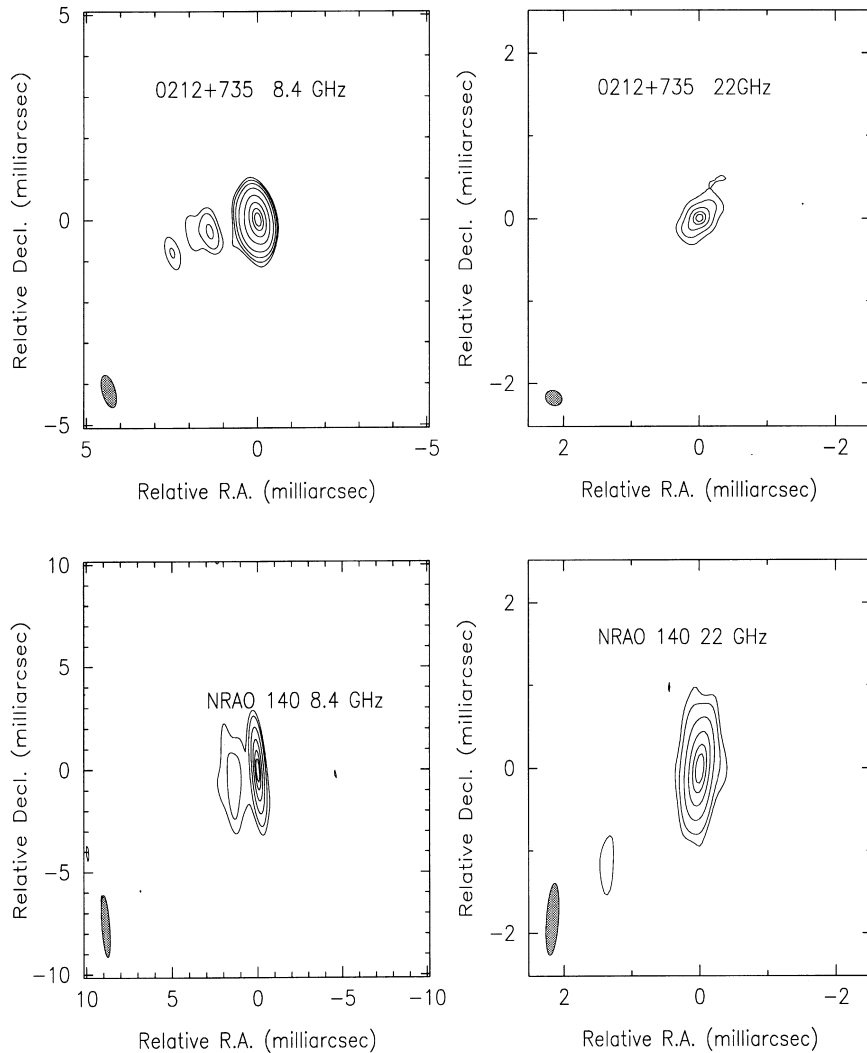


FIG. 1.—Continued

ual counts. Also, the actual N_{H} value could be smaller or larger than the assumed Galactic value (see below for a discussion of this point). It is also possible that a single power-law model is not adequate for describing this source. The first observation of 1611+343 is poorly fitted. Probably only the last reason is applicable here, since there are enough counts to determine the spectrum rather well, and the best-fit N_{H} is fairly close to the Galactic value.

In many cases the best-fit values for N_{H} are either considerably smaller or larger than the measured Galactic N_{H} . There are several likely explanations for this. If the best-fit value is larger, as is the case for 3C 120 and 0736+017, then there could be significant photoelectric absorption within the source. There could also be significant amounts of as yet unobserved Galactic molecular gas in the direction of the FSRQ. Also possible is a spectral flattening at low X-ray energies. A closer look at the photon spectrum of 3C 120 shows that the peak is poorly fitted by the model, which indicates that a single power law is probably not the best model for this source. It is also possible that the Galactic column density of hydrogen is higher (or lower) in the immediate vicinity of the FSRQ as compared to the average value over the much larger regions measured with the 2° FWHM beam of the Stark et al. (1992) survey. This seems to be the case for 3C 345, for which N_{H} measured with the

smaller beam in the Elvis, Lockman, & Wilkes (1989) study is 7.5×10^{19} , which is certainly closer to the best-fit value of N_{H} for the 1990 observation than is the value $N_{\text{Hgal}} = 3.6 \times 10^{20} \text{ cm}^{-2}$ derived from Stark et al. (1992). These possibilities have been discussed in more detail by Wilkes & Elvis (1987) and Worrall & Wilkes (1990), among others. However, the higher resolution H I observations of Elvis et al. (1989) show that N_{Hgal} is smaller than that derived from Stark et al. (1992) for 0736+017 and only 2% larger for 3C 120. It is still possible that N_{Hgal} in the immediate direction of the quasar was larger at the time of the X-ray observations, since temporal variability of N_{Hgal} cannot be excluded (see, e.g., Frail et al. 1994). For 0736+017, the inferred column density from CO observations (Liszt & Wilson 1993) is $5.6(\pm 0.8) \times 10^{20} \text{ cm}^{-2}$, which can account for the difference. This also results in a much steeper derived value of the spectral index, which is more in agreement with other low-redshift active galaxies and quasars (see discussion below). If the best-fit value of N_{H} is smaller than the Galactic value, as is the case for 0133+476, 3C 111, 1633+382, and 3C 345, then it is possible that these sources are not adequately described by a single power law. The most likely possibility is a soft X-ray excess, perhaps from thermal black body X-ray emission (from an accretion disk) with a steep slope.

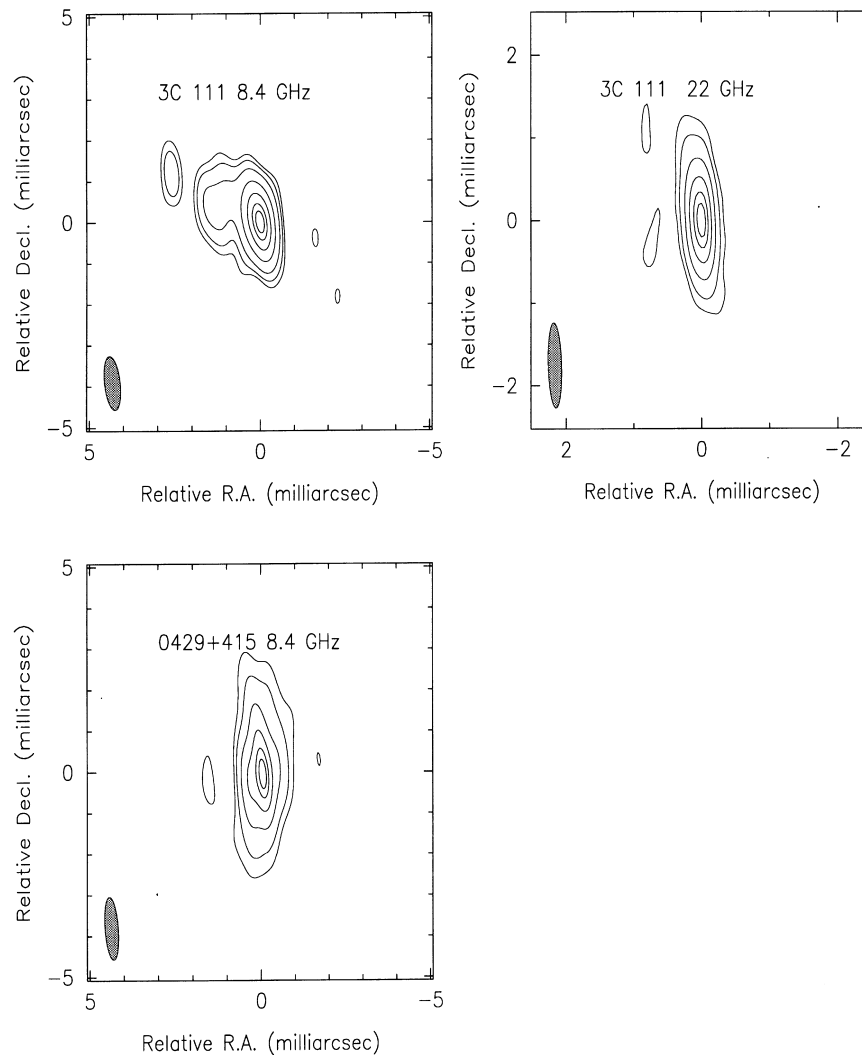


FIG. 1.—Continued

An analysis for some sources in this sample has appeared in other summaries of X-ray emission from blazars (see Comastri et al. 1997; Sambruna 1997). Most of the parameter determinations (such as spectral index and column density of hydrogen) are very similar. Our flux density values do occasionally differ, mainly because we base our flux values on best-fit parameters, whereas Sambruna (1997) use fixed N_{Hgal} to calculate flux densities. In addition, their source/background counts determination differs from ours slightly. The first observation of 1611+343 is the only case for which the flux densities differ by more than 5% (we present a value that is 50% lower).

2.5. Gamma-Ray Data

Several sources in our sample were detected with the EGRET instrument on the *Compton Gamma-Ray Observatory*. The fluxes for EGRET detected objects can be found in Thompson et al. (1995) and upper limits for some sources in the sample can be found in Fichtel et al. (1994). The dates listed in Table 1 are for the EGRET Viewing Periods, covering the area of the source, which were closest in time to the other multiwavelength observations. Calibration of the instrument and determination of fluxes are discussed in Hartman et al. (1992) and Mattox et al. (1993) and (1996), respectively.

2.6. Summary of Source Properties

Owing to incomplete time coverage, it is not possible to analyze thoroughly the variability properties of each source. However, we can discuss some general results. Of the 17 sources with repeated millimeter/submillimeter wave observations reported here and in Bloom et al. (1994), 10 (0133+476, NRAO 140, 3C 111, 0642+449, 0736+017, 0836+710, 3C 345, 2005+403, 2037+511, and 2201+315) are significantly variable at one or more wavelengths. Six of these (0133+476, NRAO 140, 0736+017, 0836+710, 3C 345, and 2201+315) are significantly variable at all measured wavelengths. The timescales are roughly 7–14 months; no source has a variability amplitude parameter that exceeds 0.5.

With the X-ray observations presented earlier, combined with observations by previous spacecraft missions (*HEAO A-1*, *Einstein*, *EXOSAT*, and *Ginga*), we have determined the crude X-ray variability characteristics of the sources in the sample, using the same criterion for significance as for the millimeter observations. We note that in some cases it is difficult to establish variability, especially if the observations being compared were made with different instruments or very different spectral fit parameters (as mentioned above). The sources appear to fall into several general categories (Malaguti, Bassani, & Caroli 1994; Bloom 1994 for

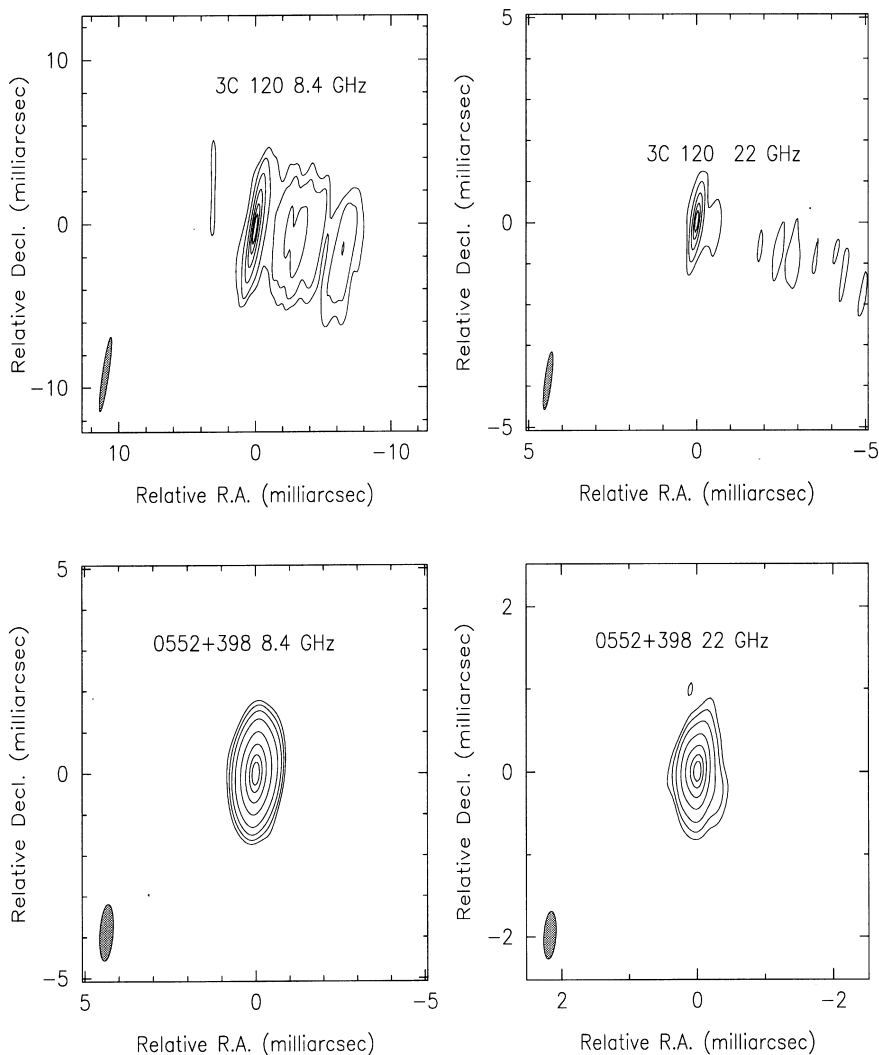


FIG. 1.—Continued

references to the published X-ray data for each source). Of the 24 sources in our sample with *ROSAT* X-ray observations, seven (0133+476, 0552+398, 0820+560, 0917+499, 0954+556, 0955+476, and 1638+398) have indeterminate X-ray variability owing to insufficient observations. For an additional seven sources (0016+731, 0642+449, 0736+017, 0804+499, 1150+812, 2136+141, and 2201+315), variability was not detected, though some of these are low-amplitude variables at millimeter wavelengths (e.g., 0736+017; see Tornikoski et al. 1994). Two sources, 0945+408 and 1633+382, are observed to be significantly variable in X-rays (and, for 1633+382, γ -rays; see Thompson et al. 1995) only, whereas three additional sources (NRAO 140, 0836+710, and 4C 39.25) show possible X-ray variability that is temporally correlated with radio or millimeter-wave variability. With each of these three sources, the millimeter flux varied by the same factor as the X-ray flux (see Marscher 1988 for NRAO 140; this work and Bloom et al. 1994 for 0836+710 and 4C 39.25). These last five sources mentioned were all variable with constant X-ray spectral index, which is typical of non-thermal processes. Five additional sources (0212+735, 3C 111, 3C 120, 1611+343, and 3C 345) had complex variability properties, such as variation in spectral index as well as intensity. All of the sources with $\lesssim 80\%$ of the VLBI flux

density in the core at 8.4 GHz are X-ray variable, falling into one of the last three categories. The possible relationship between X-ray and milliarcsecond-scale structure is discussed in § 4.2.

3. SPECTRAL ANALYSIS

3.1. Spectral Deconvolution

In this section, the radio to submillimeter and infrared spectra of Bloom et al. (1994) are used to determine the synchrotron spectral turnover frequencies for each source in the sample with sufficient data. In addition, for sources observed with both *ROSAT* and VLBI, X-ray measurements are compared with the theoretical spectra of synchrotron self-Compton (SSC) models generated by the techniques described below. For sources with published EGRET γ -ray data, those data are also included for further comparison with the theoretical spectra. The total flux density spectra presented in Bloom et al. (1994) are dissected into the spectra of individual VLBI scale components using the total flux density data and flux densities from the best-fit models to the 8.4 and 22 GHz VLBI visibilities. The emphasis of the spectral decomposition is on finding the spectral turnover frequency and flux density of the bright “VLBI core” component usually located at one end of a

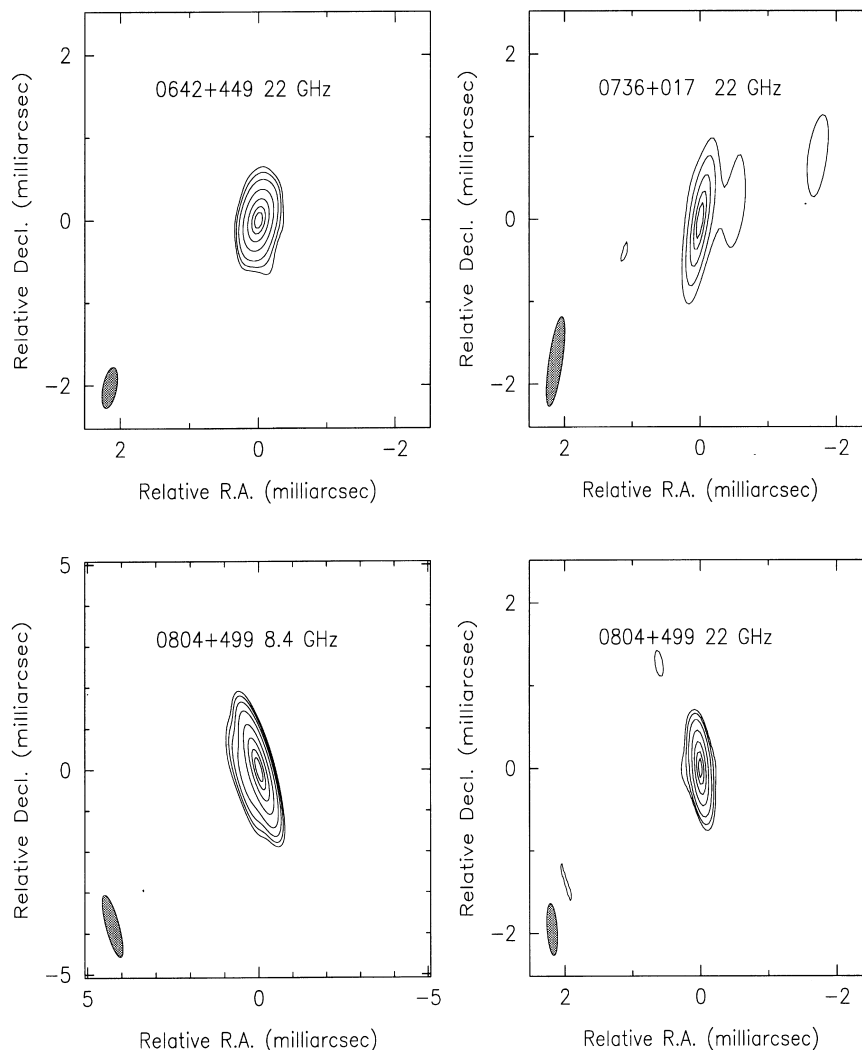


FIG. 1.—Continued

source. Owing to the limited data and the weakness of the secondary components, we do not attempt to fit the spectra of any noncore “knots” (except for the peculiar source 4C 39.25, which was analyzed by Zhang & Marscher 1994 as part of a separate study).

In Figure 3 the spectral dissection for a representative source is shown. The turnover frequency ν_m is determined from the data by first calculating the frequency ν_n at which the optically thin and optically thick spectra (of slope α_{mm} and α_{thick} , respectively) intersect (Jones, O’Dell, & Stein 1974b; Marscher 1977). In some cases this is not straightforward, since the VLBI spectra are complex (e.g., 3C 120 and 1633+382). For such sources, there is significant blending of components at 8.4 GHz that are separated in the higher resolution 22 GHz maps. There are also additional components not visible in the 22 GHz images because of overresolution and/or steep spectra. There are insufficient data to separate these components properly; thus only the 22 GHz core flux is used with the total flux density data to determine the spectral turnover. In sources with no VLBI data, best estimates are made using the total flux density data. We also note that in some cases, the VLA and/or VLBI data points exceed the values for the single-dish measurements (Fig. 3). Since it is obviously not possible for the small-scale components to have greater flux density than the entire

source seen by a single dish, these differences in flux are attributable to differences in calibration. Since all of the sources have falling millimeter and submillimeter spectra, there is a firm upper limit of 100–150 GHz to the turnover frequency. All sources in the sample have optically thick spectral indices below the turnover that are much flatter than the value of 2.5 expected from a homogeneous source. These flatter indices are indicative of sources with decreasing radial gradients in magnetic field B and electron energy distribution normalization factor N_0 . Using the expressions of Marscher (1977), who considered such cases, the actual synchrotron turnover frequency ν_m is related to the intersection value ν_n by a constant factor, which in most cases is close to unity. The quantity F_m is the turnover flux density determined by extrapolating the optically thin spectrum down to frequency ν_m . The values of ν_n , ν_m , F_m , α_{mm} , and α_{thick} for each source are listed in Table 8.

For sources observed with VLBI, the angular sizes are derived from those obtained from the models that best fit the visibilities as described in § 2.2. Though elliptical Gaussians are used to represent the brightness distribution of each source component, for the SSC calculations, the visibilities can equivalently be represented by a uniform sphere with angular diameter $\theta_{\text{us}} = 1.8(\theta_a \theta_b)^{1/2}$ (Marscher 1987). The equivalent size for a spherically symmetric, nonuniform

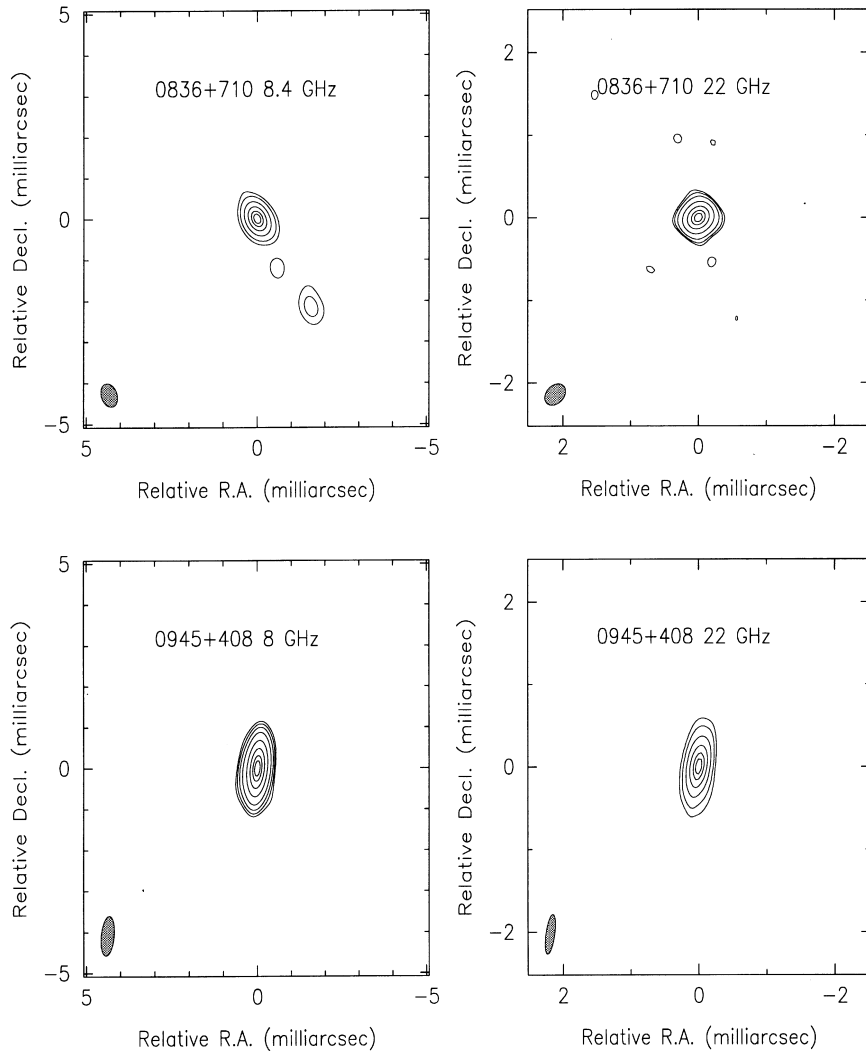


FIG. 1.—Continued

source is $(1.8k_\theta)^{-1}\theta_{\text{us}}$, where k_θ is a parameter in the range 1–2 (Marscher 1977). The value θ_{us} is used in the subsequent modeling calculations. This angular size value is strictly valid only if the core is known to be optically thin. In most cases, our spectra reveal the core to be optically thick; however, we use these optically thin values for consistency with the following Compton calculations (which assume the source is optically thin).

3.2. Synchrotron Self-Compton Calculations

Once F_m and ν_m are determined, these values as well as millimeter spectral indices and angular sizes are used with the following equation (multiplied by a constant factor; see Marscher 1987):

$$F_v^{1C} \propto \theta^{-2(2\alpha_{\text{mm}}+3)} F_m^{2(\alpha_{\text{mm}}+2)} \nu_m^{-3\alpha_{\text{mm}}+5} E_{\text{keV}}^{-\alpha_{\text{mm}}} \ln\left(\frac{\nu_2}{\nu_m}\right) \times \left(\frac{1+z}{\delta}\right)^{2(\alpha_{\text{mm}}+2)}. \quad (3.2.1)$$

Here, ν_2 is the upper cutoff frequency to the synchrotron spectrum, and δ is the Doppler factor corresponding to bulk relativistic motion. We use equation (3.2.1) to predict the X-ray flux density at 1 keV under the initial assumption that there is no relativistic beaming ($\delta = 1$). The angular

sizes used in this equation should be measured at the turnover frequency. In general this is not the case, since VLBI observations were undertaken at only 8.4 and 22 GHz, below ν_m for most sources. In the case of a turnover frequency $\nu_m > 22$ GHz, the measured angular size is expected to follow the inequality $\theta(\nu) > \theta(\nu_m)$, and the Compton flux is underestimated. If the source is transparent at 22 GHz, then the measured angular size is acceptable. For sources with IR data, the cutoff frequency ν_2 can be estimated and is typically $\sim 10^{14}$ Hz. Otherwise, this frequency is assumed to be 10^{14} Hz.

In a number of cases the X-ray flux densities predicted in this way are much greater than those measured. If relativistic beaming is taken into account, a minimum Doppler factor can be derived from the measured and predicted X-ray flux densities:

$$\delta_{\text{min}} = \left(\frac{F_{\text{vx,obs}}}{F_{\text{vx,pred}}}\right)^{-1/[2(\alpha_{\text{mm}}+2)]}. \quad (3.2.2)$$

The best estimate of the Doppler factor is then used with the initial estimate of the X-ray flux density to generate model first- and second-order SSC spectra. Model spectra for selected FRSQs with minimum Doppler factors obtained from the SSC calculations are shown in Figure 4 (0133+476) and Figure 5 (0836+710). The parameters used

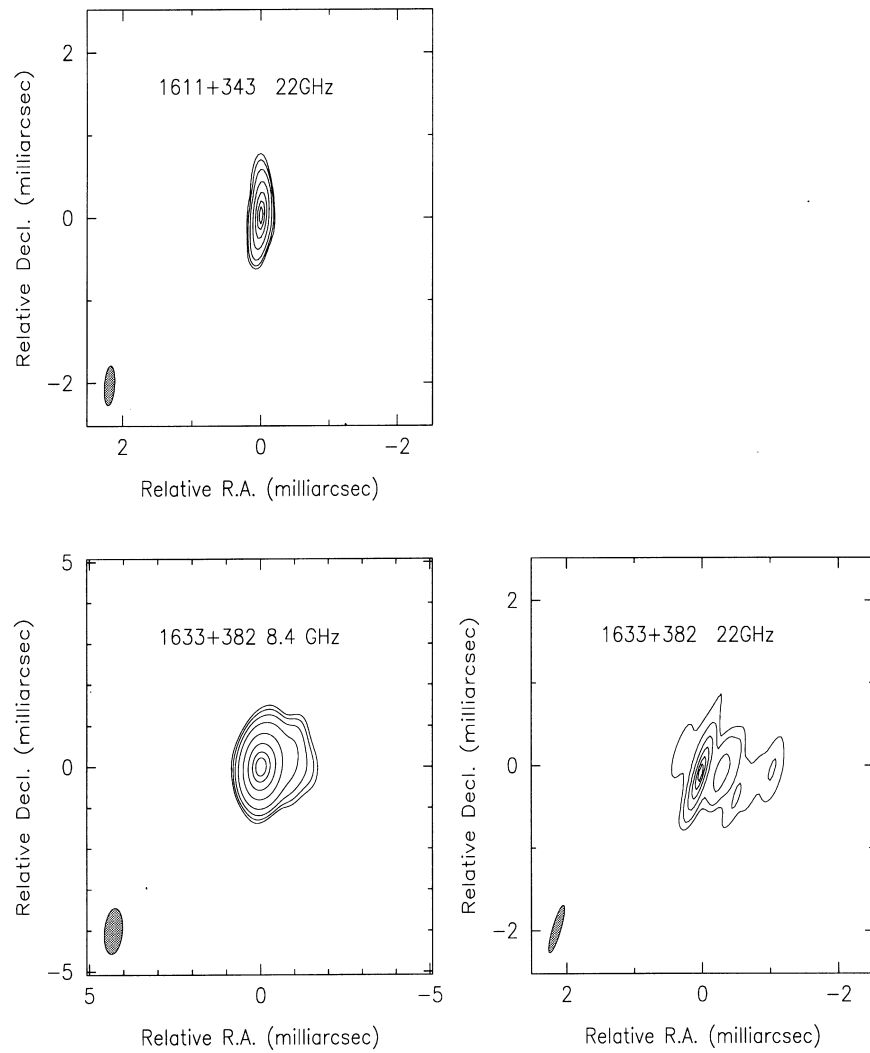


FIG. 1.—Continued

to generate the models are listed in Table 9. The SSC calculations show that seven of 16 sources observed with both VLBI and *ROSAT* have predicted X-ray flux densities at 1 keV greater than the observed values. The resolution of this discrepancy requires relativistic beaming of the radiation.

To evaluate more clearly what these predictions mean, we can roughly estimate the uncertainty in the SSC predicted flux and the Doppler factor using standard propagation of errors techniques (i.e., Bevington 1969, p. 204). Though this strictly holds only for parameters that have normal distributions and symmetric errors, a meaningful result for the uncertainty can be evaluated if we treat the terms of equations (3.2.1) and (3.2.2) logarithmically:

$$\sigma_{\text{tot}}^2 = a^2 \sigma_{\log \theta}^2 + b^2 \sigma_{\log F}^2 + c^2 \sigma_{\log \nu}^2 + \dots \quad (3.2.3)$$

Here, σ_{tot} refers to the total logarithmic uncertainty in the predicted Compton flux. a , b , and c refer to the powers involving spectral index that appear in equation (3.2.1). The corresponding subscripts refer to angular size, maximum synchrotron flux density, and the spectral turnover frequency. There are then other smaller or unquantifiable terms that we have not written down (but we discuss them below). Following this technique, and assuming approximately 50% errors in the angular size, 40% errors in the turnover flux and frequencies, and a spectral index of approximately 0.7, the uncertainty in $\log F_{\text{vx,pred}}$ is about 2.

Realistically, since the spectral index itself can be uncertain by a few percent, and since there are very likely to be correlated error terms which we have not included, this number could be closer to 3. Though correlated error terms could also reduce the overall uncertainty, in the absence of more information we feel that it is wise to adopt the larger number. This number corresponds to a “worst case scenario.” As discussed earlier in § 2.2, some of the VLBI data have angular sizes with uncertainty as small as 13%. The resulting uncertainty would be smaller by more than an order of magnitude in those cases (~ 50). However, in general, overestimations of the Compton flux, are significant only if this is an overevaluation by more than 3 orders of magnitude. By this standard, all of the overestimates in Table 9, except for 0133+476, are marginal; however, many of the underestimates are not. Using similar analysis on δ_{min} and realizing the $F_{\text{vx,pred}}$ is the main contribution to the uncertainty, we calculate that the uncertainty in the log of the minimum Doppler factor is about 0.3. Thus, we conclude that the uncertainties are too large, generally, to determine whether Compton scattering and Doppler beaming are necessary to reconcile predictions with the X-ray data.

In some cases the X-ray spectral slopes predicted by the SSC mechanism disagree with the slopes determined from fits to the *ROSAT* data. This could be due to non-SSC

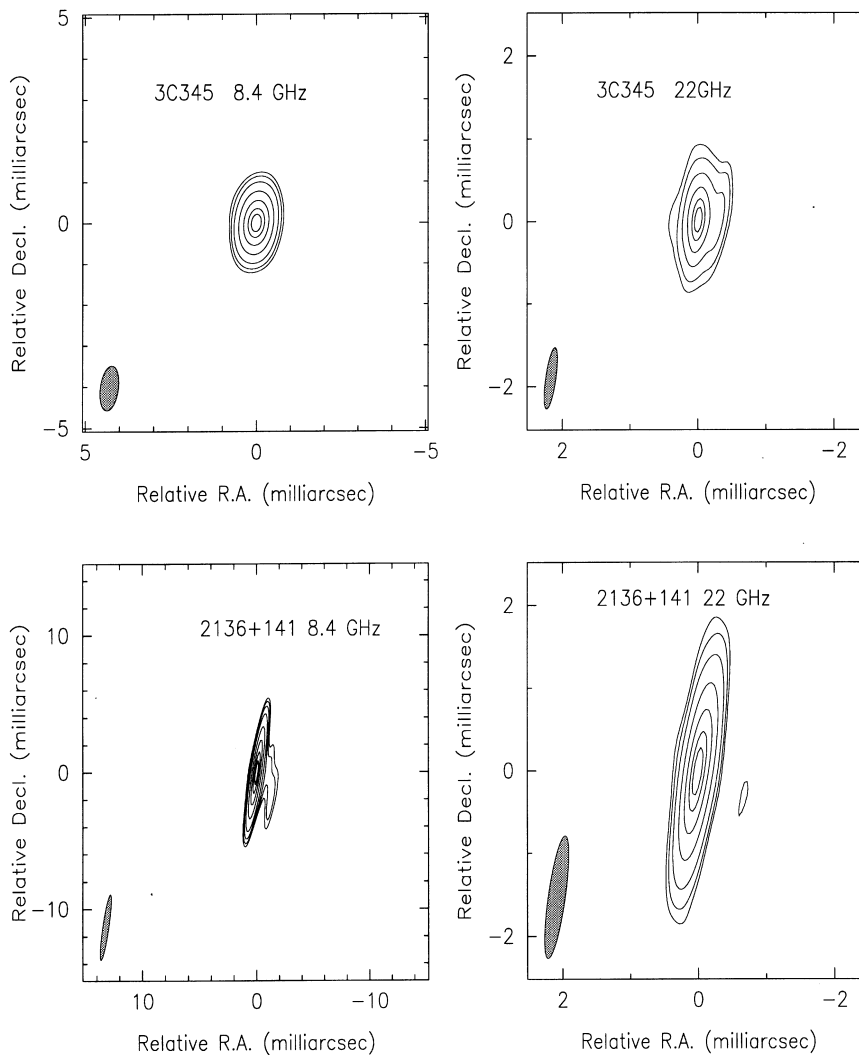


FIG. 1.—Continued

contributions (e.g., from a “soft X-ray excess” component) or simply a poorly derived X-ray spectrum arising from the limited energy range to which the ROSAT PSPC is sensitive. Nonuniform models (e.g., shock waves in which the electrons suffer radiative losses; Marscher & Gear 1985) can produce self-Compton X-ray spectra that are flatter than the optically thin synchrotron spectra.

For 0836+710, the γ -ray spectrum of 1992 March is roughly in agreement with the predicted composite first- and second-order multiwaveband spectrum (Fig. 5). These results are similar, in general, but not in detail, with the modeling results for 0836+710 presented by Comastri et al. (1997). The model predicts that the source should have become faint at γ -ray energies by 1992 October–November, and indeed no detection was reported when the source was next observed in early 1993 (Thompson et al. 1995). This illustrates the value of contemporaneous multiwaveband observations in testing models: source variability invalidates tests based on noncontemporaneous measurements.

In addition to modeling the spectra, we use observed synchrotron parameters, such as F_m , v_m , α , v_2 , and θ , in Table 10 to determine physical parameters such as N_0 and B . These results show that the magnetic field B ranges from 1×10^{-2} to $140 (\delta_{\min}/\delta)$ G and N_0 from 9×10^{-13} to $2 \times 10^{-3} (\delta/\delta_{\min})^{2(\alpha+2)}$ (cgs units).

For sources previously observed to exhibit superluminal motion, the range of possible values for the Doppler factor derived from the apparent transverse velocities v_{app} can be compared to those derived using equation (3.2.2). Known superluminal sources with measured X-ray fluxes lower than the predicted values tend to have minimum required values of δ that are compatible with the observed values of v_{app}/c , as should normally be the case: 0836+710 ($v_{\text{app}}/c = 15 h^{-1}$ [Krichbaum et al. 1990], $\delta > 3$), 4C 39.25 ($v_{\text{app}}/c = 3.5 h^{-1}$, $\delta > 5.2$ [Marscher et al. 1991], and 3C 345 ($v_{\text{app}}/c = 8 h^{-1}$, $\delta > 2.1$; see Unwin et al. 1994). (Here we adopt the values $q_0 = 0$ and $H_0 = 100 h \text{ km s}^{-1} \text{ Mpc}^{-1}$.) However, this need not be the case for all sources, since the value of δ can be high while v_{app}/c is low for jets pointing essentially along the line of sight. In such cases, the jet should not appear as extended as in the high- v_{app}/c sources.

4. STATISTICAL ANALYSIS

We use correlation and linear regression to test for and to model approximately the bivariate relationships among the data. We employ these techniques with emphasis on those parameters most likely to be related to X-ray emission and γ -ray emission. Since the SSC process predicts a specific relationship between high-energy flux densities, radio flux density, spectral turnover frequency, and angular size, these

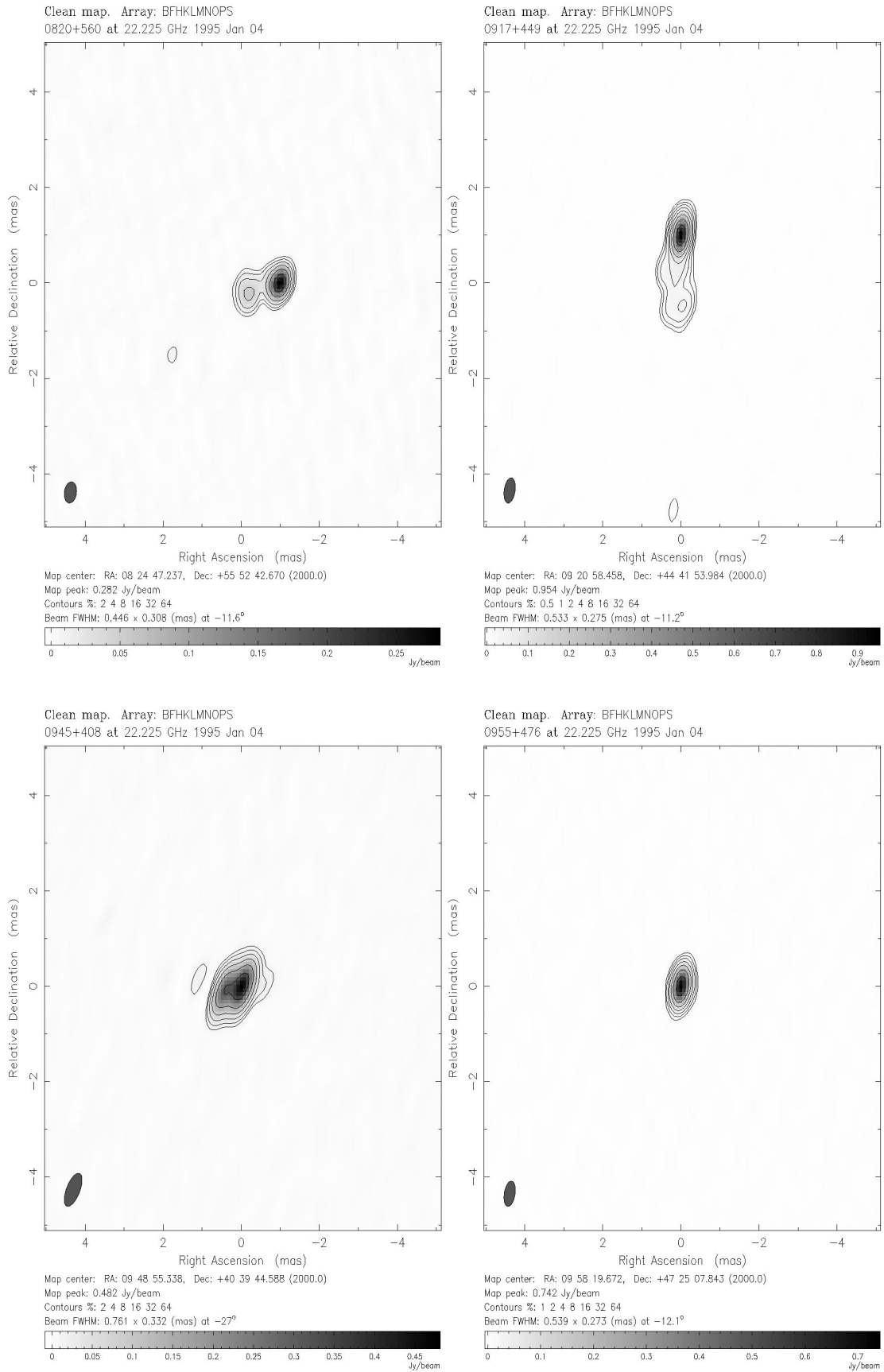


FIG. 2.—VLBA images at 22 GHz

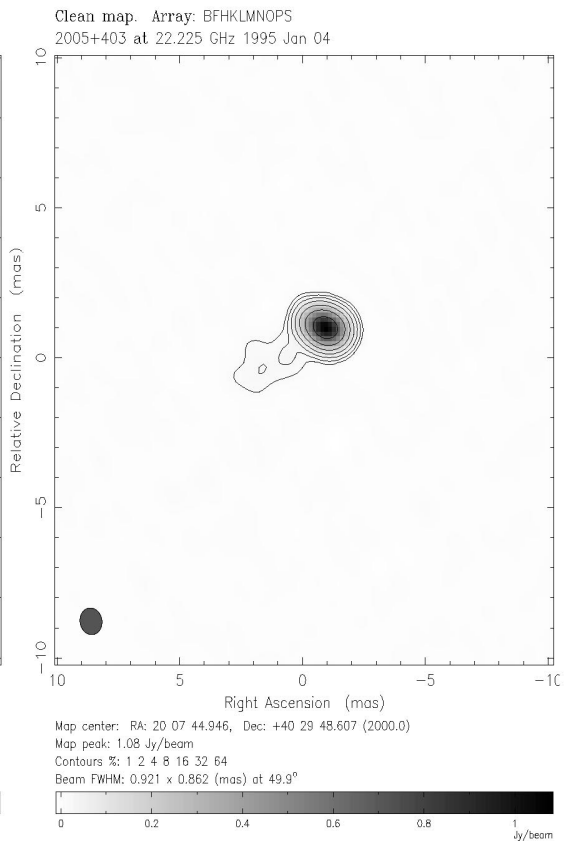
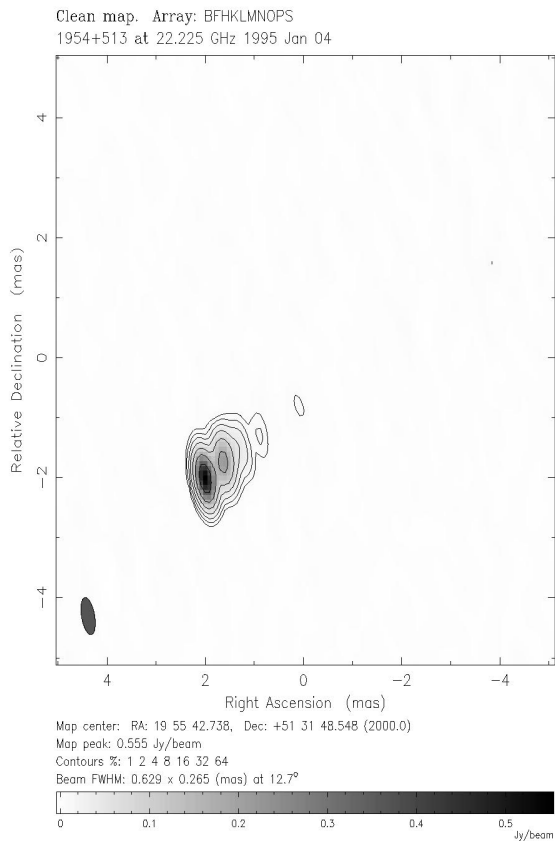
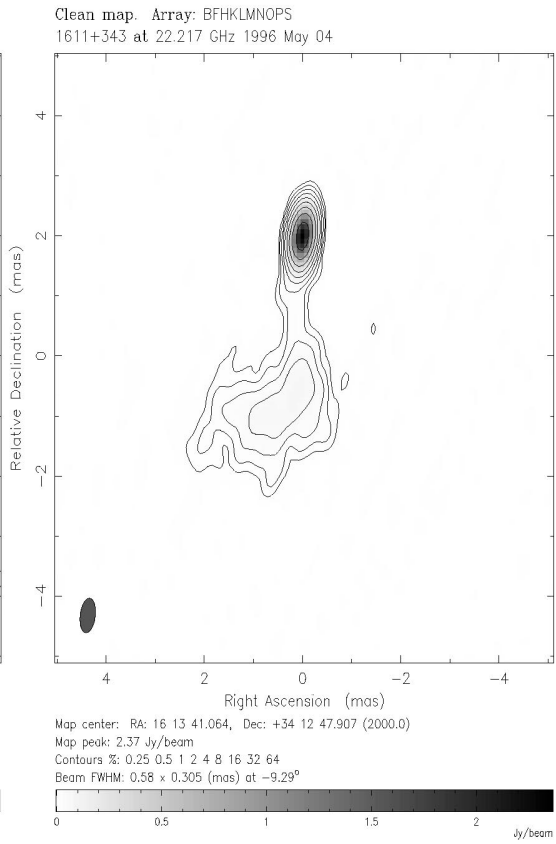
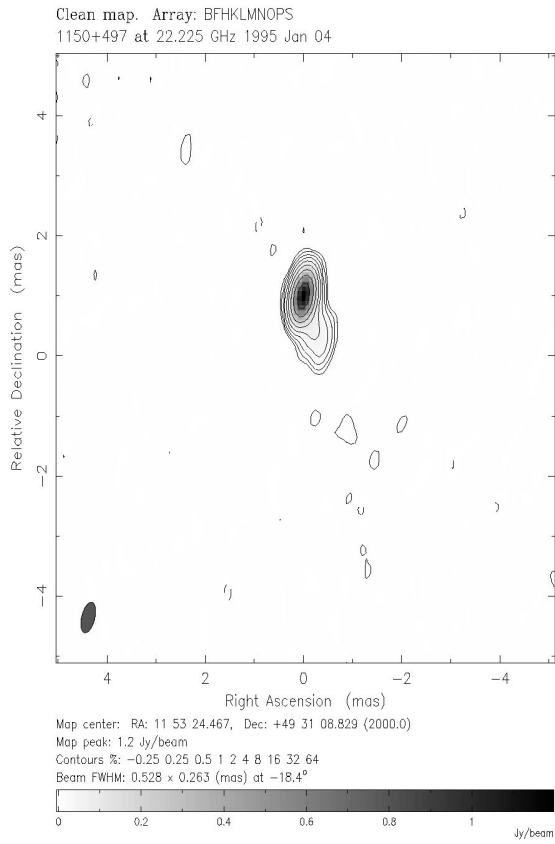


FIG. 2.—Continued

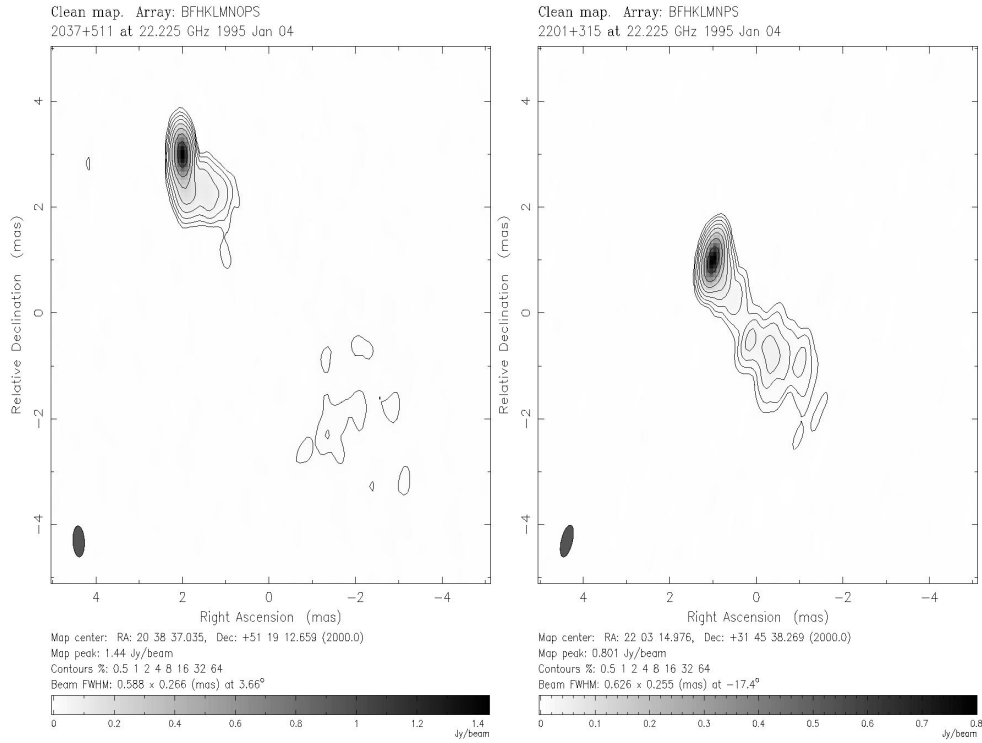


FIG. 2.—Continued

parameters are studied most closely. In addition, other parameters such as the X-ray and millimeter-wave spectral indices, and VLBI compactness, are examined.

All of the luminosities in this section are calculated assuming $q_0 = 0$ and $H_0 = 100 h \text{ km s}^{-1} \text{ Mpc}^{-1}$, with h arbitrarily chosen to be 0.75.

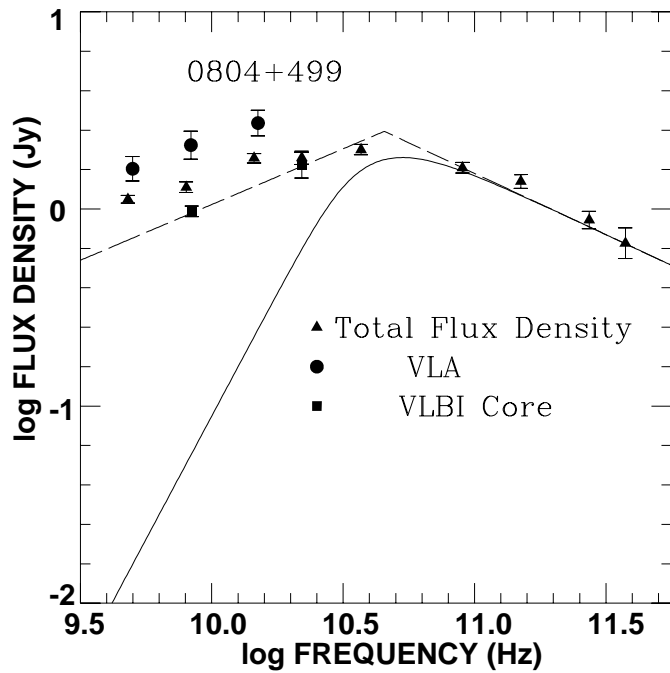


FIG. 3.—Determination of the turnover frequency from VLBI and total flux density data. The dotted lines show the frequency ν_n at which the extrapolation of the partially opaque and optically thick spectra meet. The solid curve is the synchrotron spectrum for a homogeneous sphere with spectral turnover at frequency ν_n , as discussed in the text.

4.1. Survival Analysis—Correlation and Regression

Owing to the presence of upper and lower limits to some of the measured or inferred quantities (data with limits are often referred to as “censored” data), survival analysis techniques are used to evaluate more accurately correlation coefficients (with their associated probabilities) and regression slopes (see Isobe, Feigelson, & Nelson 1986). In general, these techniques take into account censored data by assuming a form for the distribution of the censored values relative to the measured ones. The ASURV Rev 1.1 statistical software package is used to calculate correlation properties for censored data (Isobe & Feigelson 1990). As

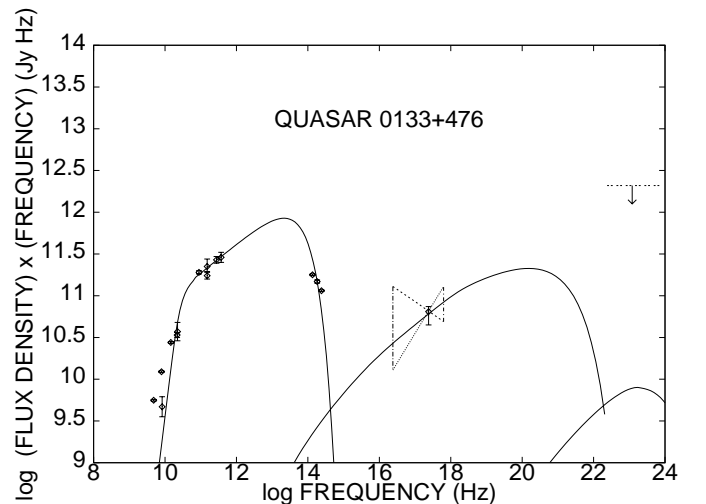


FIG. 4.—The synchrotron spectrum (fitted by a self-absorbed, uniform source model) and predicted first-order (*middle curve*) and second-order (*rightmost curve*) spectra for 0133+476, plotted against the contemporaneous data.

TABLE 5
MILLIMETER/SUBMILLIMETER OBSERVATIONS WITH THE JCMT^a

Source (1)	Date (2)	Wavelength (μ m) (3)	Flux Density (Jy) (4)	Variable? ^b (5)
0736+017	1993 Nov 21	800	1.13 ± 0.08	0.2
		1100	1.27 ± 0.08	0.3
		1300	1.48 ± 0.11	...
		2000	1.70 ± 0.10	0.3
0917+449	1993 Dec 08	800	0.84 ± 0.10	No
		1100	0.95 ± 0.10	No
		1300	1.01 ± 0.10	...
		2000	1.19 ± 0.15	No
0923+392 (4C 39.25).....	1993 Dec 08	800	0.48 ± 0.06	No
		1100	2.46 ± 0.17	No
		1300	2.79 ± 0.15	...
		2000	3.62 ± 0.45	No
0945+408	1993 Dec 08	800	<0.39	No
		1100	...	No
		1300	0.39 ± 0.10	No
		2000	0.59 ± 0.13	No
0954+556	1993 Dec 08	800	<0.23	No
		1100	0.16 ± 0.04	No
		1300	0.20 ± 0.04	No
		2000	0.47 ± 0.08	No
0955+476	1993 Dec 08	800	0.21 ± 0.07	No
		1100	0.23 ± 0.05	No
		1300	0.40 ± 0.05	No
		2000	0.44 ± 0.08	No
1641+399 (3C 345).....	1993 Sep 14	800	1.35 ± 0.12	0.4
		1100	1.85 ± 0.07	0.3
		1300	2.24 ± 0.10	...
		2000	2.9 ± 0.15	0.3
2005+403	1993 Sep 14	800	0.23 ± 0.07	...
		1100	0.29 ± 0.05	0.3
		1300	0.47 ± 0.08	No
		2000	0.70 ± 0.14	No
2201+315	1993 Sep 14	1100	0.40 ± 0.07	0.3
		1300	0.41 ± 0.06	0.3
		2000	0.60 ± 0.13	0.3

^a See Bloom et al. 1994 for data from earlier epochs.

^b $(F_{\max} - F_{\min})/(F_{\max} + F_{\min})$; "No," if variability is not significant, as defined in text.

pointed out by Isobe et al. (1986), spurious correlations (or spurious null correlations) can occur if these limits are disregarded.

There are many correlation tests and linear regression methods. In general, since they are both nonparametric, the Spearman rank correlation coefficient and Kendall's τ are best suited to test for correlation among two variables for which the nature of the parent distributions is unknown. The Spearman rank coefficients are provided in the summary of our results in Table 11.

The Buckley-James method (BJ) is used for determining regression coefficients. This method is preferred over other methods, since it does not assume a Gaussian distribution of the residuals about the regression line. In cases for which there are limits present in the independent variable (e.g., the possible dependence of X-ray flux density on angular size), only Schmitt's regression method (SB) can be used. However, this method is not considered preferable for general use, since it involves arbitrary binning of the data. (For a more detailed discussion of the relative merits of these methods, see Isobe et al. 1986.) When no limits are present, the regression results are nearly identical to the

results from standard methods (see, e.g., Bevington 1969, p. 204).

Since several previous studies have shown a strong correlation between X-ray and radio luminosities for radio-loud quasars (e.g., Worrall et al. 1987), we examine this relationship first. We consider separately the correlation between X-ray luminosity and radio core luminosity, X-ray and millimeter luminosity at 270 GHz, and X-ray and radio luminosity at spectral turnover. The analogous relationships between the flux densities as well as between the flux density at each wave band and redshift are studied, to ascertain whether the luminosity correlations are intrinsic or spurious.

As can be seen in Figures 6, 7, 8, 9, 10, and 11, the X-ray and millimeter flux densities are correlated, the X-ray and radio core flux densities are uncorrelated, and the X-ray and turnover flux densities are weakly correlated. All of the luminosity-luminosity plots in these figures show moderate or strong correlations. The X-ray/millimeter relationship may be stronger than that of the X-ray/core because the core is optically thick. Optically thick synchrotron emission makes only a very small contribution to the total soft radi-

TABLE 6
INFRARED OBSERVATIONS WITH UKIRT^a

Source (1)	Date (2)	Wavelength (μm) (3)	Flux Density (mJy) (4)	α_{IR} (5)	Instrument (6)	
0804 + 499	1993 Nov 19	1.25	1.70 ± 0.06	-0.01	UKT9	
		1.65	1.81 ± 0.07			
		2.20	1.69 ± 0.04			
.....	1994 Mar 5	1.25	0.33 ± 0.01	0.06	UKT9	
		1.65	0.41 ± 0.03			
		2.20	0.37 ± 0.03			
0820 + 560	1993 Dec 09	1.25	0.30 ± 0.02	0.63	UKT9	
		1.65	0.42 ± 0.04			
		2.20	0.43 ± 0.03			
0923 + 392 (4C 39.25).....	1993 Nov 19	1.25	1.59 ± 0.03	0.38	UKT9	
		1.65	1.43 ± 0.03			
		2.20	1.97 ± 0.07			
0945 + 408	1994 May 13	1.25	0.33 ± 0.06	0.90	IRCAM	
		1.65	0.45 ± 0.09			
		2.20	0.55 ± 0.11			
	1994 May 17	1.25	0.30 ± 0.06	0.97	IRCAM
			1.65	0.39 ± 0.08		
			2.20	0.52 ± 0.10		
0954 + 556	1993 Dec 09	1.25	0.77 ± 0.02	0.94	UKT9	
		1.65	0.96 ± 0.03			
		2.20	1.31 ± 0.04			
0955 + 476	1993 Dec 09	1.25	0.71 ± 0.03	1.61	UKT9	
		1.65	1.05 ± 0.05			
		2.20	1.76 ± 0.07			
1641 + 399 (3C 345).....	1993 Sep 15	1.25	1.03 ± 0.01	1.51	UKT9	
		1.65	1.48 ± 0.06			
		2.20	2.42 ± 0.06			
2005 + 403	1993 Sep 15	1.25	0.29 ± 0.02	0.66	UKT9	
		1.65	0.33 ± 0.02			
		2.20	0.42 ± 0.04			
2201 + 315	1993 Sep 15	1.25	3.99 ± 0.03	1.52	UKT9	
		1.65	5.48 ± 0.03			
		2.20	9.39 ± 0.05			

^a See Bloom et al. 1994 for data from earlier epochs.

ation field that is upscattered to X-ray energies (Band & Grindlay 1986). A summary of the correlation and regression analysis is given in Table 11. Regression results are given only if the probability that a correlation is not present is less than 20%.

If the correlation between the luminosities were due solely to the common distance factors used to derive them, then the regression slope would be close to unity. However, the regression slope is less than 1 in all cases. Isobe et al. (1986) show through Monte Carlo simulations of data from flux-limited samples that if the underlying physical relationship between the luminosities is of the form $L_2 = KL_1^\alpha$, then luminosity diagrams will reflect this through the regression slope, as long as upper limits are included in the analysis. The resulting flux-flux plots show a correlation with considerably steeper slopes. Although the underlying physical relationship between the luminosities in this sample is likely to be more complex than the one assumed by Isobe et al. (1986), their results do indicate that, for some forms of luminosity functions, the data will show the intrinsic correlation in the luminosity-luminosity plots even if the sample has a distance-luminosity bias. To evaluate the possibility of spurious luminosity correlations due to common redshift factors, we have used the partial correlation methods of Padovani (1992). This analysis calculates the correlation

between two variables, while effectively removing the effects of other known variables. We find that there is still a moderate correlation between L_X and both L_{mm} and L_c ($\rho_s = 0.28$ and 0.39 , respectively), after the correlations of each luminosity with redshift have been negated. However, the partial correlation between L_X and L_m is weak, which indicates that the apparent relationship between these two luminosities found earlier is probably spurious. The results are not strongly affected if the extremely low redshift objects 3C 111 and 3C 120 are removed from the sample (as is seen in Table 11).

Figures 12, 13, 14, 15, 16, and 17 give correlation plots and histograms of various other interesting observational parameters. Owen et al. (1981) used the histogram of the effective millimeter to X-ray spectral index to show that the X-ray fluxes are closely linked to the millimeter fluxes. Bloom & Marscher (1991) showed that this also holds in general for the radio cores of quasars, even though the observations were often separated by years. Figure 15 shows that this is also true for the present sample, with millimeter and X-ray observations separated by 6 months at most. Inspection of Figure 12 and Tables 11 and 12 shows that there is a weak anticorrelation between X-ray spectral index and both millimeter and infrared spectral indices. This would tend to show that a harder component

TABLE 7
X-RAY SPECTRAL PARAMETERS

Source (1)	Date (2)	Counts (0–2.5 keV) (3)	Observing Time (s) (4)	$\log N_{\text{H,gal}}$ (atoms cm^{-2}) (5)	$\log N_{\text{H,best}}$ (atoms cm^{-2}) (6)	α	$F_{1\text{keV}}$ (μJy) (7)	χ^2 (8)	dof (9)
0016+731	1992 Jul 29	40 ± 7	5243	21.38	...	1.0	0.06 ± 0.01	6.9	12
0133+476	1992 Aug 12	285 ± 17	4036	21.37	20.92 ^{+0.08} _{-0.12}	0.66 ^{+0.64} _{-0.36}	0.27 ^{+0.10} _{-0.04}	14	25
0212+735 ^a	1991 Feb 16	308 ± 18	7210	21.39	...	-0.60 ± 0.40	0.20 ^{+0.02} _{-0.03}	9	8
NRAO 140 ^b	1992 Aug 8	921 ± 31	4039	21.41	21.46 ± 0.02	1.01 ^{+0.16} _{-0.17}	1.59 ^{+1.11} _{-0.61}	33	30
C 111 ^b	1991 Mar 8	265 ± 17	838	22.08	...	2.25 ^{+0.65} _{-0.40}	12.3 ^{+1.9} _{-2.2}	7	17
	1993 Feb 13	840 ± 29	2322	22.08	21.98 ± 0.02	1.48 ± 0.20	8.4 ^{+10.3} _{-4.4}	16	25
3C 120	1991 Feb 20	3642 ± 62	1724	21.03	21.54 ± 0.02	2.13 ^{+0.09} _{-0.11}	18.4 ^{+4.6} _{-3.9}	36	25
0552+398	1993 Mar 13	185 ± 14	4294	21.28	...	0.09 ^{+0.36} _{-0.16}	0.21 ± 0.03	12	21
0642+449	1991 Mar 13	73 ± 10	3108	20.79	...	0.79 ^{+0.86} _{-0.59}	0.08 ^{+0.01} _{-0.02}	20	22
0736+017	1991 Apr 3	234 ± 16	1936	21.08	...	1.24 ^{+0.36} _{-0.14}	0.50 ^{+0.06} _{-0.05}	21	20
	1992 Apr 6	396 ± 20	3296	21.08	...	1.45 ^{+0.25} _{-0.45}	0.47 ^{+0.06} _{-0.05}	24	20
0804+499	1992 Oct 27	144 ± 12	2999	21.32	...	1.09 ^{+0.71} _{-0.79}	0.24 ^{+0.11} _{-0.07}	44	30
>0836+710 ^a	1992 Mar 3	5365 ± 75	6990	20.46	20.54 ± 0.05	0.57 ± 0.11	2.37 ± 0.10	41	41
	1992 Nov 2	1904 ± 44	5030	20.46	20.56 ± 0.10	0.57 ^{+0.19} _{-0.18}	1.21 ^{+0.08} _{-0.09}	15	15
0917+449	1993 Oct 27–Nov 3	639 ± 28	3225	20.55	20.53 ± 0.10	0.94 ^{+0.30} _{-0.24}	0.49 ^{+0.25} _{-0.20}	40	31
0923+392 ^c	1991 Apr 15	741	...	20.23	20.20 ± 0.20	1.17 ^{+0.38} _{-0.34}	0.52 ± 0.06
	1993 Apr 22	1356	...	20.23	20.30 ^{+0.16} _{-0.20}	1.32 ± 0.30	0.69 ^{+0.07} _{-0.06}
0945+408	1993 Nov 10	189 ± 16	2577	20.16	...	1.06 ^{+0.22} _{-0.24}	0.09 ± 0.02	46	31
0954+556	1993 Nov 8	393 ± 24	4293	19.95	19.92 ^{+0.28} _{-0.40}	1.30 ^{+0.45} _{-0.30}	0.08 ± 0.02	53	31
0955+476	1993 Nov 13	339 ± 20	3450	20.01	...	0.19 ^{+0.15} _{-0.26}	0.21 ^{+0.05} _{-0.04}	45	31
1150+812 ^a	1992 Apr 7	58 ± 9	2930	20.65	...	0.55 ^{+0.21} _{-0.25}	0.09 ^{+0.09} _{-0.10}	13	5
	1992 May 7	172 ± 14	5650	20.65	...	(Combined)
	1992 Oct 29	241 ± 17	9500	20.65	...	0.41 ^{+0.19} _{-0.29}	0.09 ^{+0.10} _{-0.09}	5.4	4
1611+343	1992 Sep 30	418 ± 21	3651	20.45	20.32 ^{+0.08} _{-0.12}	1.34 ± 0.30	0.15 ^{+0.03} _{-0.01}	80	30
	1993 Jan 17	332 ± 18	3153	20.45	20.30 ^{+0.15} _{-0.23}	0.65 ± 0.35	0.24 ^{+0.04} _{-0.03}	16	24
1633+382	1992 Aug 20	1208 ± 38	5781	20.58	20.18 ^{+0.12} _{-0.16}	0.76 ^{+0.17} _{-0.20}	0.41 ^{+0.04} _{-0.03}	41	30
1638+398	1992 Sep 3	64 ± 9	2857	20.49	...	1.89 ± 0.30	0.04 ± 0.01	15	15
3C 345	1990 Jun 19	1193 ± 43	4086	20.56	19.71 ^{+0.20} _{-0.40}	0.77 ^{+0.13} _{-0.17}	0.39 ^{+0.04} _{-0.03}	54	30
	1992 Jun 16	1014 ± 40	3899	20.56	20.11 ^{+0.14} _{-0.21}	0.91 ^{+0.24} _{-0.25}	0.51 ± 0.05	41	30
2136+141	1991 May 9	147 ± 16	4076	20.93	...	0.50 ^{+0.50} _{-0.70}	0.12 ± 0.02	22	20
2201+315	1993 May 12	553 ± 25	3329	21.09	21.29 ^{+0.11} _{-0.14}	2.00 ^{+0.90} _{-0.70}	3.78 ^{+0.62} _{-0.58}	14	32

^a From Brunner et al. 1994.

^b N_{H} is atomic and molecular.

^c From Zhang et al.

to the X-ray emission is visible when the synchrotron spectrum is steep and is not contributing as much to the X-ray flux via the SSC mechanism. This finding is somewhat surprising, since we would expect that sources with less significant SSC emission would then be dominated by the softer (steeper) spectrum of an accretion disk, though, since several of the sources with the steepest millimeter spectral indices are at high redshift, it could be that the softest X-rays from an accretion disk are redshifted out of the *ROSAT* band. The anticorrelations of the spectral indices are especially interesting considering that the fluxes in the millimeter and X-ray wave bands (and the luminosities) are correlated. It would be hard to argue in favor of the SSC mechanism (at least in a simple form) if these correlations are observed in the future for simultaneous data from a large set of objects. However, without detailed X-ray spectral analysis of individual sources (which will have to await *AXAF*), it is difficult to analyze this result much further. There is also a strong correlation between α_{mmx} and VLBI core fraction at 8.4 GHz, as seen in Figure 16. Here, core fraction is defined to be the fraction of total milliarcsecond-scale flux density (as determined by model fitting) that is in the core component. Note that there is one outlying point, which corresponds to 3C 120. Even with 3C 120 excluded, the correlation is highly significant, and the regression rela-

tion remains similar to the earlier case. The correlation weakens at 22 GHz (Fig. 17). Although this may be due to the inferior calibration at high frequencies, it is also true that the jet (as opposed to core) components tend to be weaker, and the core stronger, at 22 GHz than at lower frequencies. The correlation suggests that more X-rays are created for a given millimeter-wave luminosity if jet components are more prominent. That sources with more prominent jet components should be brighter at high energies was also suggested by Wehrle & Mattox (1994) in their correlation between VLBI structure and γ -ray detections, although their result was of marginal statistical significance. It is certainly not expected if the bulk of the high-energy emission comes from the quiescent jet, as in the Ghisellini, Maraschi, & Treves (1985) model.

There are various explanations for this correlation. If the bulk Lorentz factors for each source are similar, then the sources with smaller angles between the jet axis and the line of sight will have larger Doppler beaming factors. Such sources will be more severely foreshortened as viewed by the observer, and thus the jet “knot” components will not be as easily detected (because of blending with the core) as for jets that are less highly beamed. This effect will also tend to decrease the SSC X-ray flux for a given millimeter flux (all other quantities, such as turnover frequency, being

TABLE 8
SPECTRAL DISSECTION PARAMETERS

Source (1)	ν_n (2)	ν_m (3)	F_m (4)	α_{mm} (5)	α_{thick} (6)
0016+731.....	60	54	1.94	1.36	0.33
0133+476.....	42	37	3.80	0.65	1.13
0212+735.....	64	58	1.99	1.57	0.0
NRAO 140.....	78	69	2.92	1.35	0.38
3C 111.....	79	73	4.28	0.75	0.81
3C 120.....	67	67	2.63	0.80	0.41
0552+398.....	39	47	4.35	1.06	0.0
0642+449.....	75	65	4.09	1.81	0.0
0736+017.....	58	78	1.95	0.84	0.12
0804+499.....	45	57	2.15	0.63	0.56
0836+710.....	27	33	1.34	0.90	0.21
0923+392.....	...	8	4.5	0.52	...
0945+408.....	33	33	1.73	0.72	0.0
0954+556.....	19	28	0.88	0.65	0.28
1611+343.....	47	51	3.18	0.65	0.88
1633+382.....	74	94	1.82	0.60	0.56
3C 345.....	48	53	8.98	0.60	0.90
1954+513.....	27	38	2.52	0.65	0.35
2005+403.....	37	26	4.18	0.92	1.58
2037+511.....	31	50	3.88	0.63	0.11
2136+141.....	19	15	1.63	0.77	0.27
2201+315.....	26	21	4.32	0.70	1.47

roughly equal; see eq. [3.2.1]). Recent VLBI and X-ray observations of 3C 345 (Unwin et al. 1997) indicate that there are states in which the X-ray emission emanates from the jet and not the nucleus, as one might normally expect. At these times the relative contribution of radio flux from the extended jet is much higher. However, we note that α_{mmx} was uncorrelated with the core fraction as this particular flare progressed in 3C 345.

Another possible explanation is that the sources with less prominent jets have wider opening angles, so knots expand rapidly, which would decrease their SSC emission. If this is the case, such sources should be found to be more highly variable (at least in the decay stages of flares) than those

with prominent jets. It may also be that the sources with strong jets are in an enhanced state (e.g., from shock compression), which would increase the ratio of X-ray to millimeter flux as compared to the other sources. However, for several individual sources (NRAO 140, 0836+710, and 4C 39.25), this ratio seems to be preserved during flares. As mentioned in § 2, long-term X-ray variability appears to be related to 8.4 GHz VLBI structure as well, though this information is probably too limited. In the Melia & Königl (1989) model, the X-rays arise from inverse Compton scattering of seed photons from an accretion disk by relativistic electrons deep in the jet. Because of the geometry of the scattering, the X-ray emission is lower along the jet axis

TABLE 9
COMPTON CALCULATION PARAMETERS

Source (1)	z (2)	ν_m (3)	F_m (4)	α_{mm} (5)	θ (6)	$F_{vx,pred}$ (7)	$F_{vx,obs}$ (8)	δ_{min} (9)
0016+731.....	1.76	54	1.94	1.36	0.67	5.1×10^{-8}	0.06	0.13
0133+476.....	0.86	37	3.80	0.65	$\lesssim 0.08$	$\gtrsim 2.6 \times 10^5$	0.27	14
0212+735.....	2.37	58	1.99	1.57	0.36	7.3×10^{-7}	0.20	0.17
NRAO 140.....	1.26	69	2.92	1.35	0.52	4.3×10^{-7}	1.59	0.11
3C 111.....	0.05	73	4.28	0.75	0.50	1.0×10^{-5}	12.3	0.08
3C 120.....	0.03	67	2.63	0.80	$\lesssim 0.46$	$\gtrsim 1.5 \times 10^{-6}$	18.4	0.06
0552+398.....	2.3	47	4.35	1.06	0.47	4.6×10^{-2}	0.21	0.79
0642+449.....	3.40	65	4.09	1.81	0.32	0.03	0.06	0.89
0736+017.....	0.19	58	1.74	0.84	$\lesssim 0.35$	$\gtrsim 8.4 \times 10^{-6}$	0.50	0.15
0804+499.....	1.43	45	2.49	0.63	$\lesssim 0.21$	$\gtrsim 8.28$	0.24	2.0
0836+710.....	2.17	27	1.80	0.90	$\lesssim 0.17$	$\gtrsim 7.1 \times 10^2$	1.2	3.0
0923+392.....	0.70	8	4.5	0.52	0.54	2.2×10^3	0.52	5.2
0945+408.....	1.25	54	1.28	0.72	0.58	3.0×10^{-6}	0.09	0.15
0955+476.....	1.87	65	0.70	0.97	0.32	2.1×10^{-6}	0.21	0.14
1611+343.....	1.40	45	3.17	0.65	0.27	2.8	0.15	1.7
1633+382.....	1.81	94	1.23	0.6	0.33	6.7×10^{-5}	0.41	0.19
3C 345.....	0.60	48	9.33	0.6	$\lesssim 0.31$	$\gtrsim 24$	0.51	2.1
2136+141.....	2.45	15	1.63	0.77	$\lesssim 0.42$	$\gtrsim 18$	0.12	2.5
2201+315.....	0.30	21	4.10	0.70	0.41	2.0	3.78	0.89

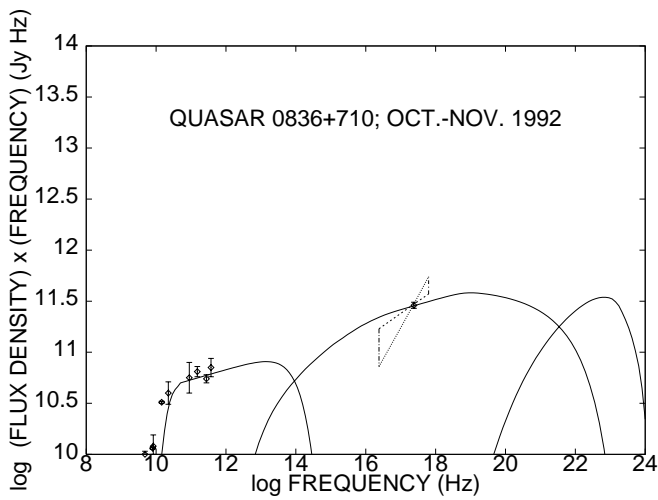
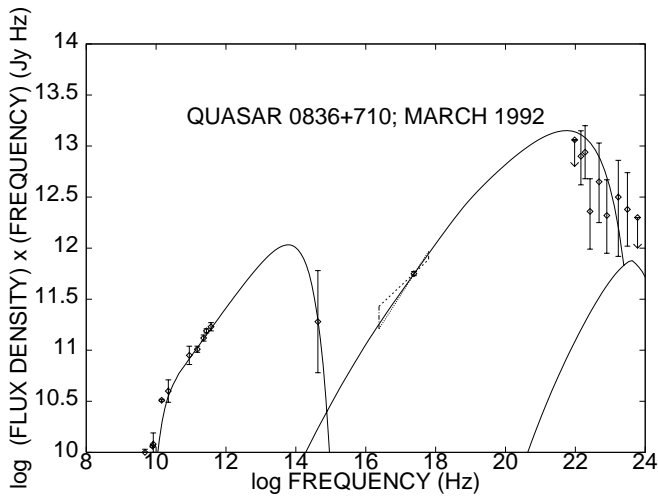


FIG. 5.—Similar to Fig. 4, except for the quasar 0836+710. The EGRET gamma-ray data from Thompson et al. (1993) are plotted to the right on the 1992 March spectrum. Optical data are from von Linde et al. (1993). The large uncertainty in the optical point corresponds to the range of fluxes during a short-term flare.

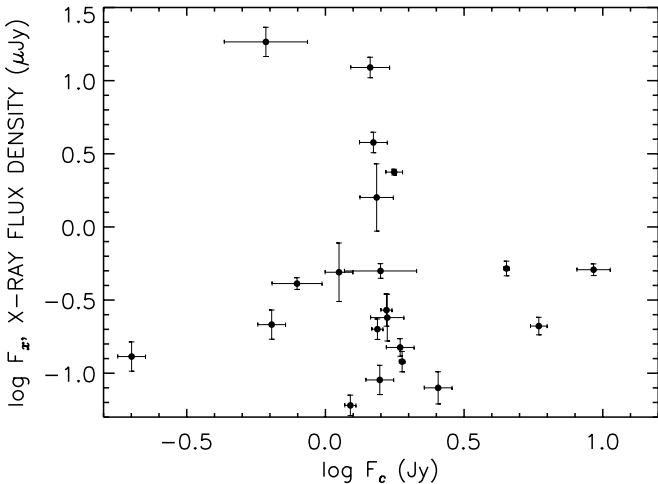


FIG. 6.—Correlation plot between VLBI core flux density at 22 GHz and X-ray flux density at 1 keV.

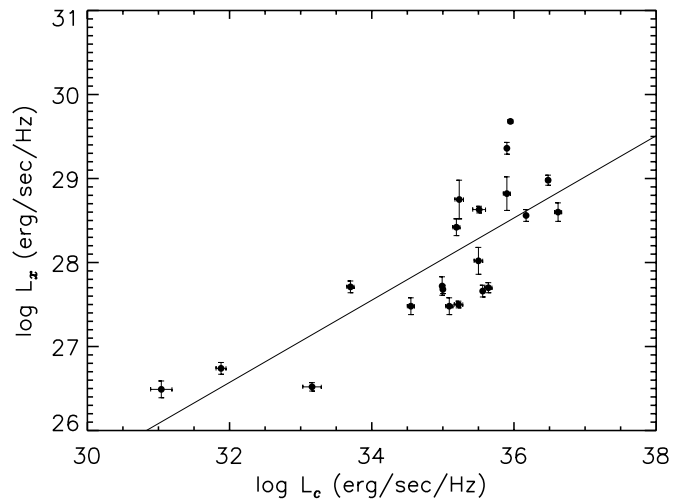


FIG. 7.—VLBI core luminosity at 22 GHz vs. X-ray luminosity at 1 keV. The solid line corresponds to a linear regression.

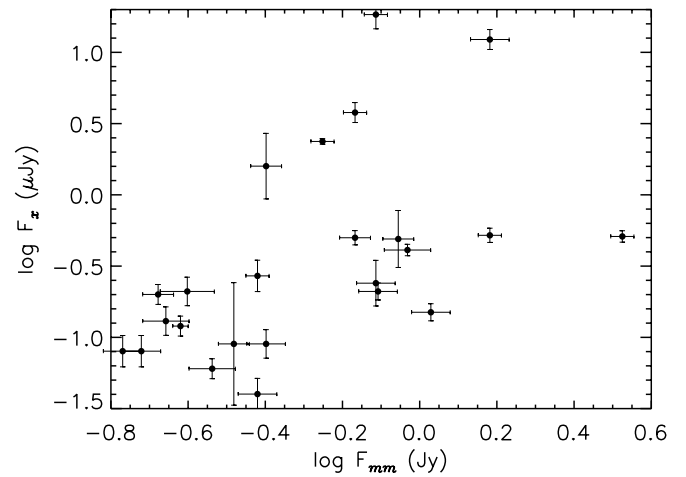


FIG. 8.—Millimeter-wave flux density (273 GHz) vs. X-ray flux density at 1 keV.

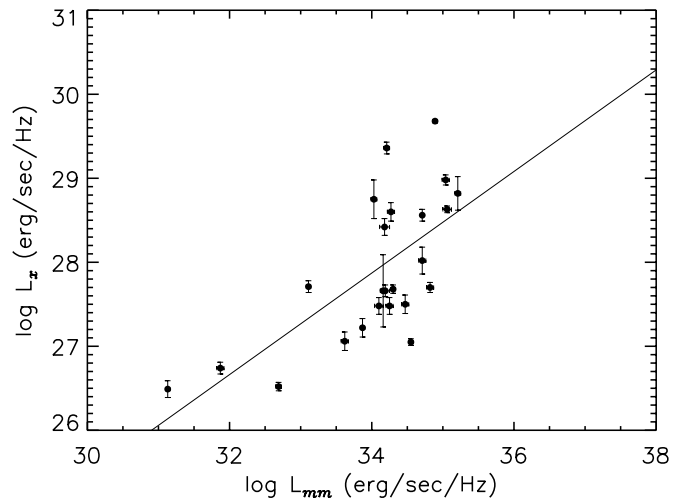


FIG. 9.—Millimeter-wave luminosity (273 GHz) vs. X-ray luminosity at 1 keV.

TABLE 10
 PHYSICAL PARAMETERS

Source (1)	$B(\frac{\delta_{\min}}{\delta})$ (2)	$N_0(\frac{\delta}{\delta_{\min}})^{2(\alpha+2)}$ (3)	R (4)	γ_{\min} (5)	γ_{\max} (6)	α_{1c} (7)
0016+731	41	1×10^{-11}	4.2	~ 10	3×10^3	1.37
0133+476	$\lesssim 6 \times 10^{-2}$	$\lesssim 5 \times 10^{-6}$	$\lesssim 0.41$	~ 10	$\lesssim 8 \times 10^3$	0.66
0212+735	17	6×10^{-12}	2.4	~ 10	5×10^3	1.59
NRAO 140	24	2.6×10^{-11}	3.1	~ 10	5×10^3	1.35
3C 111	21	5×10^{-5}	0.33	~ 10	4×10^3	0.76
3C 120	$\lesssim 20$	$\lesssim 7 \times 10^{-5}$	$\lesssim 0.19$	~ 10	$\lesssim 5 \times 10^3$	0.81
0552+398	5	2.3×10^{-9}	3.1	~ 10	4×10^3	1.06
0642+449	6	8.5×10^{-13}	4.6	~ 10	4×10^3	1.85
0736+017	$\lesssim 16$	$\lesssim 7.2 \times 10^{-7}$	$\lesssim 0.75$	~ 10	$\lesssim 3 \times 10^3$	0.93
0804+499	$\lesssim 2$	$\lesssim 1 \times 10^{-6}$	$\lesssim 1.3$	~ 10	$\lesssim 3 \times 10^3$	0.66
0836+710	$\lesssim 1 \times 10^{-1}$	$\lesssim 1 \times 10^{-6}$	$\lesssim 1.1$	~ 100	$\lesssim 1 \times 10^4$	0.76
0923+392	1×10^{-2}	2×10^{-5}	2.6	~ 10	2×10^4	0.54
0945+408	80	2.5×10^{-7}	3.5	~ 10	2×10^3	0.78
0955+476	47	6.3×10^{-8}	2.1	~ 10	3×10^3	0.99
1611+343	3	1×10^{-6}	1.6	~ 10	4×10^3	0.62
1633+382	140	6.5×10^{-6}	2.1	~ 10	2×10^3	0.68
3C 345	$\lesssim 1$	$\lesssim 2 \times 10^{-6}$	$\lesssim 1.4$	~ 10	$\lesssim 4 \times 10^3$	0.65
2136+141	$\lesssim 1 \times 10^{-1}$	$\lesssim 3 \times 10^{-7}$	$\lesssim 2.8$	~ 10	1×10^4	0.78
2201+315	0.18	2.0×10^{-5}	1.2	~ 10	1×10^4	0.70

than at a small angle (roughly the inverse of the Lorentz factor of the jet); viewed from this angle, the jet components would have maximum visibility.

There are no significant correlations between X-ray flux density and the other parameters used to predict the X-ray flux. This is somewhat surprising since one might expect strong correlations from relations such as equation (3.2.1). A lack of correlation between X-ray flux density and angular size can, however, be understood since many of the angular sizes are actually upper limits, and other angular sizes may represent the blending of two or more components. Furthermore, the actual angular sizes at the turnover frequency are likely to be smaller than those measured at 22 GHz (see § 3). The weak correlation between X-ray flux density and turnover frequency can be understood

since many of the turnover frequencies are determined with limited data and are approximate. This uncertainty would then also be exacerbated by an inaccurately determined turnover flux density. Of course, the simplest explanation for all of these noncorrelations is that the X-ray flux is not SSC in origin, and thus none of the correlations would be strong. If this is the case, the actual Doppler factors must exceed the minimum values obtained from the SSC analysis (Table 9).

4.2. Distributions

The histograms of the observed properties of FSRQs show which values are most common among the objects. These reveal both selection effects and the physical aspects of the objects, as is demonstrated below. The distribution of

 TABLE 11
 CORRELATION AND REGRESSION PARAMETERS

Dependent (1)	Independent (2)	N (3)	Percent Censored (4)	Spearman (5)	Probability (6)	Slope (7)	Intercept (8)	Method (9)
$\log F_{vx}$	$\log F_{vc}$	21	0	-0.130	0.5614
$\log L_{vx}$	$\log L_{vc}$	21	0	0.789	0.0004	0.49 ± 0.09	10.91	BJ
$\log L_{vx}$	$\log L_{vc}$	19	0	0.717	0.0023	0.67 ± 0.14	4.35	BJ
$\log F_{vx}$	$\log F_{vmm}$	24	0	0.342	0.1007	0.38 ± 0.37	-0.38	BJ
$\log L_{vx}$	$\log L_{vmm}$	24	0	0.651	0.0018	0.60 ± 0.14	7.32	BJ
$\log L_{vx}$	$\log L_{vmm}$	22	0	0.548	0.0120	0.80 ± 0.24	0.72	BJ
$\log F_{vx}$	$\log F_{vm}$	24	17	0.342	0.1007	0.85 ± 0.45	-0.85	SB
$\log L_{vx}$	$\log L_{vm}$	24	17	0.670	0.0013	0.53 ± 0.10	5.27	SB
$\log L_{vx}$	$\log L_{vm}$	22	18	0.570	0.0091	0.73 ± 0.17	2.56	SB
$\log F_{vx}$	$\log \theta$	21	29	-0.234	0.2954
$\log F_{vx}$	$\log v_m$	24	19	0.168	0.4300
$\log L_{vx}$	z	24	0	0.741	0.0004
$\log L_{vc}$	z	21	0	0.917	<0.0001
$\log L_{vm}$	z	24	17	0.857	<0.0001
$\log L_{vmm}$	z	24	0	0.705	0.0007
α_X	α_{mm}	24	0	-0.163	0.4343
α_X	α_{ir}	13	0	-0.335	0.2463
α_{IR}	α_{mm}	15	0	-0.125	0.6394
θ	$\log v_m$	24	42	0.127	0.5146

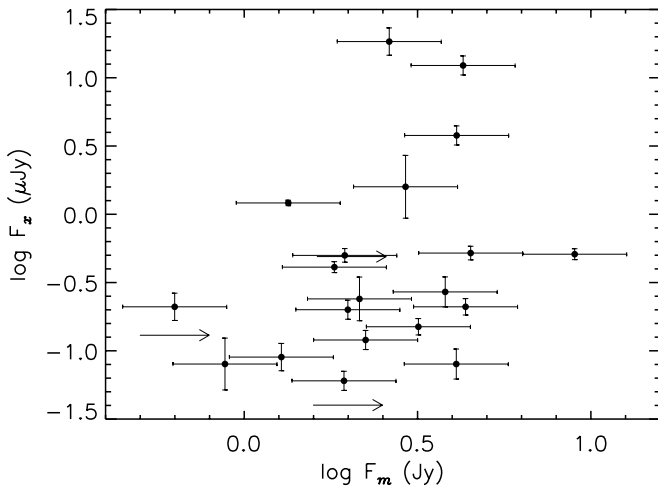


FIG. 10.—Flux density at the turnover frequency ν_m vs. X-ray flux density at 1 keV.

turnover frequencies (Fig. 13) shows a very broad peak at roughly 50 GHz, similar to that found by Gear et al. (1994). The distribution cuts off well below 150 GHz at high frequencies.

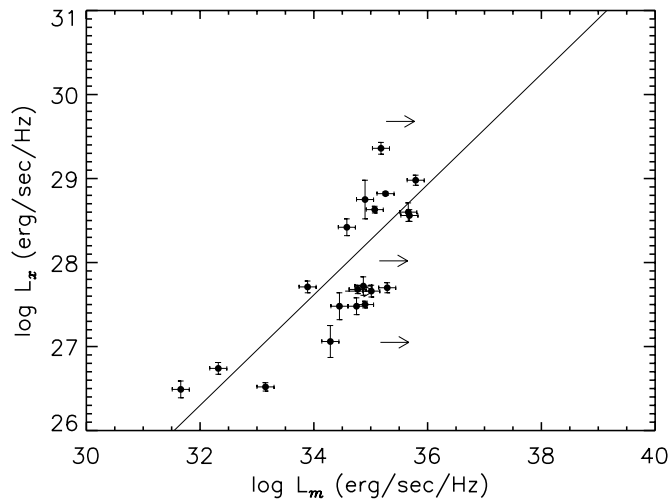


FIG. 11.—Luminosity at the turnover frequency ν_m vs. X-ray luminosity at 1 keV. The solid line is a linear regression.

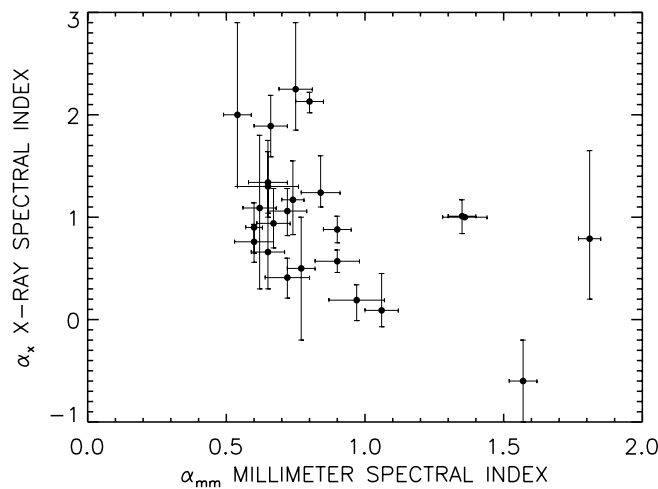


FIG. 12.—X-ray spectral index vs. millimeter-wave spectral index

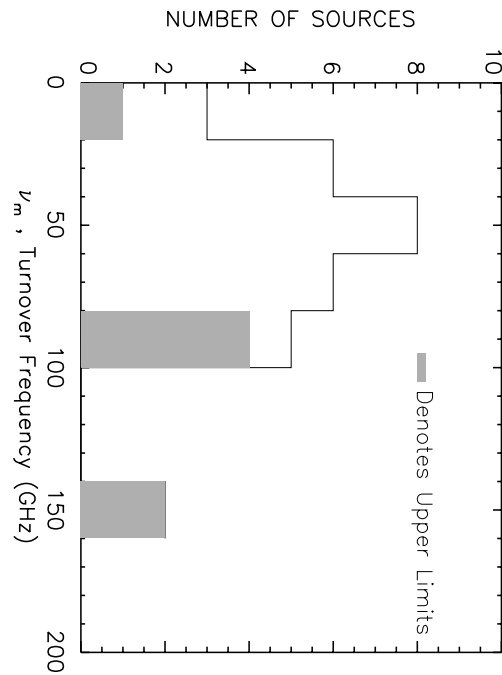


FIG. 13.—Histogram of turnover frequencies ν_m

If the flat spectra are caused by a jet with radial gradients in magnetic field and electron density (Marscher 1977 discusses the spherical case; see Marscher 1980; Königl 1981 for application to jets), then the angular size of the emission region, observed in the partially opaque portion of the spectrum, decreases inversely (the precise dependence is a function of the gradients in B and N) with frequency up to the spectral turnover. Thus, the spectral turnover frequencies are indicators of the innermost radius of the source. That the spectral turnovers occur at frequencies ~ 50 GHz, rather than up to an order of magnitude higher (as has been observed for some BL Lac objects and flaring quasars; see Brown et al. 1989; Gear et al. 1994) indicates that the smallest radius is farther out from the central engine than is implied for these other sources. The relationship $\theta_m \propto \theta_{22}(\nu/22 \text{ GHz})^{-k_2}$ is used to approximate the size of the

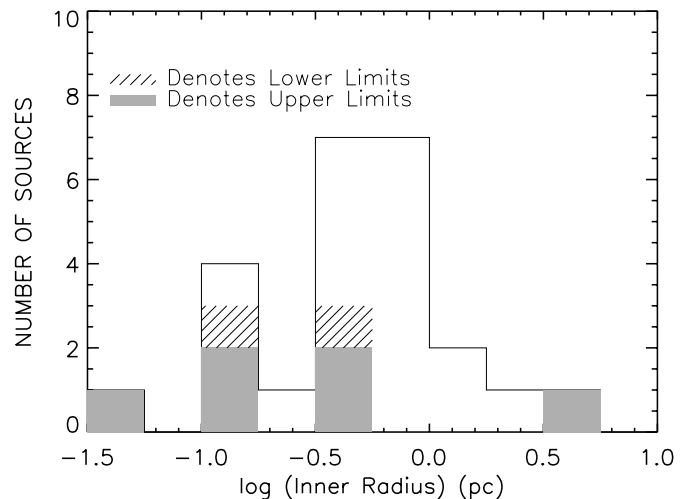


FIG. 14.—Histogram of innermost radius measured by our 22 GHz VLBI observations.

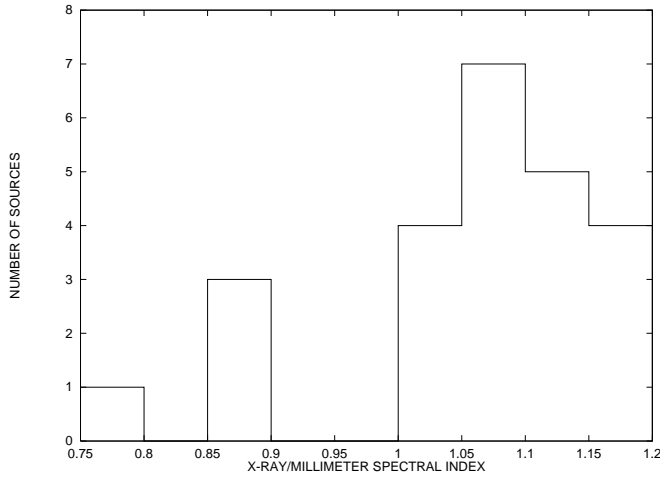


FIG. 15.—Histogram of X-ray to millimeter-wave spectral index, defined as $\alpha_{\text{mmx}} = \log(F_X/F_{\text{mm}})/\log(2.4 \times 10^{17}/2.7 \times 10^{11})$.

inner core for the sources in our sample, where θ_{22} is the angular size measured at 22 GHz. If that size is an upper limit, a value equal to half of the upper limit is used. The exponent k_2 is a constant of order unity that depends on the

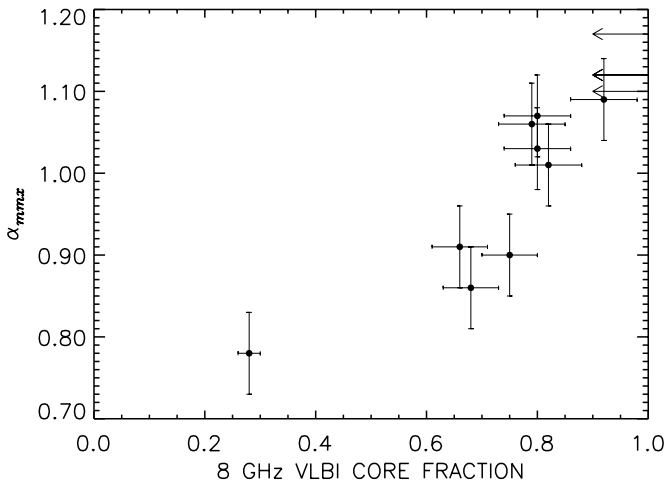


FIG. 16.—X-ray to millimeter-wave spectral index α_{mmx} vs. radio core fraction at 8.4 GHz.

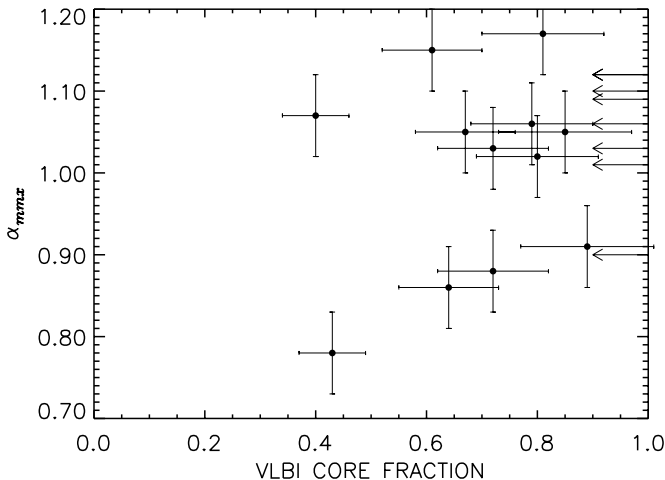


FIG. 17.—X-ray to millimeter-wave spectral index α_{mmx} vs. radio core fraction at 22 GHz.

TABLE 12
COMPARISON OF SPECTRAL INDICES

Source (1)	α_{mm} (2)	α_X (3)
0016+731.....	1.36	1.00 ^a
0133+376.....	0.65	$0.66^{+0.64}_{-0.36}$
0212+735.....	1.57	-0.60 ± 0.40
NRAO 140.....	1.35	$1.01^{+0.16}_{-0.17}$
3C 111.....	0.75	$2.25^{+0.65}_{-0.40}$
3C 120.....	0.80	$2.13^{+0.09}_{-0.11}$
0552+398.....	1.06	$0.09^{+0.36}_{-0.16}$
0642+449.....	1.81	$0.79^{+0.86}_{-0.59}$
0736+710.....	0.84	$1.24^{+0.36}_{-0.14}$
0804+499.....	0.62	$1.09^{+0.71}_{-0.79}$
0820+560.....	0.90	$0.88^{+0.13}_{-0.13}$
0836+710.....	0.90	0.57 ± 0.11
0917+449.....	0.67	$0.94^{+0.30}_{-0.24}$
4C 39.25.....	0.74	$1.17^{+0.38}_{-0.34}$
0945+408.....	0.72	$1.06^{+0.22}_{-0.24}$
0954+556.....	0.65	$1.30^{+0.45}_{-0.30}$
0955+476.....	0.97	$0.19^{+0.15}_{-0.20}$
1150+812.....	0.72	$0.41^{+0.19}_{-0.29}$
1611+343.....	0.65	1.34 ± 0.30
1633+382.....	0.60	$0.76^{+0.17}_{-0.20}$
1638+398.....	0.66	1.89 ± 0.30
1641+399.....	0.60	$0.90^{+0.24}_{-0.25}$
2136+141.....	0.77	$0.50^{+0.50}_{-0.70}$
2201+315.....	0.54	$2.00^{+0.90}_{-0.70}$

^a Assumed value for spectral index.

optically thick spectral index and is enumerated in Marscher et al. (1977). A histogram of this estimated “innermost radius” is provided in Figure 14. The peak in the distribution of turnover frequencies (see Fig. 13) is an indicator of the peak in the histogram of the inner radius at ~ 0.6 pc. However, considering our previous discussions (§ 2.2; §§ 3.1–3.2) regarding the uncertainty of the angular size, assuming an optically thin/thick source, and possible blending of components, we warn that this number should be seen as a rough estimate of where a physical change in the jet should take place and not as a canonical number. The physical meaning of this inner radius is discussed in § 5 below.

The distribution of millimeter spectral indices (see Table 12) has a sharp peak at ~ 0.7 and is clearly skewed toward steeper spectral indices.

5. DISCUSSION

We have shown that the high-energy properties of FSRQs are related to their radio to infrared properties. In particular, the millimeter–X-ray luminosity correlation is strong, as found in previous studies. In addition, we find an anticorrelation between X-ray flux and VLBI core dominance, which suggests that the knots that comprise the observed radio jets in FSRQs contribute substantially to the X-ray emission.

That the distribution of spectral indices peaks near $\alpha_{\text{mm}} \approx 0.7$ indicates that most of the sources contain a distribution of relativistic electrons with a canonical $E^{-2.4}$ spectrum. However, several sources have much steeper millimeter-wave spectral indices, as expected for radiative energy losses, or emission from an inhomogenous jet (Marscher 1980). This point is further borne out by the

infrared observations. Of the 15 sources for which we have obtained infrared data (reported here in Table 6 and in Bloom et al. 1994), six show infrared spectral indices that are 0.5–1.0 steeper than the millimeter-wave spectral indices, which is again consistent with the basic predictions for radiative energy losses. However, seven sources have infrared spectral indices that are flatter by similar amounts, probably because of another (thermal?) emission component becoming prominent toward higher frequencies.

The combined peaks in the distributions of spectral turnover frequency and angular size are shown above to indicate a characteristic size of about 0.6 pc for the radio cores of the FSRQs observed with VLBI. In an inhomogeneous jet model with radially decreasing magnetic field and electron energy normalization, the synchrotron turnover frequency is predicted to increase with decreasing radius (Marscher 1980; Ghisellini et al. 1985). Hence, if jets extended down to some arbitrarily small radius, this would result in much higher observed turnover frequencies. Thus, there is clearly some physical inner cutoff to the radio jet. The exact nature of this is unknown. There could be a change in geometry at this radius. That is, the jet could make a transition from a conical geometry to one which has a weaker dependence on radius, such as a paraboloid (see, e.g., Marscher 1980). Magnetic field and electron density, and therefore the turnover frequency, would then depend less strongly on radius. This transition in geometry could be caused by a change in the external pressure on the jet or the cooling of the protons to nonrelativistic mean internal energies. A change in Doppler factor along the jet, either from a change in jet speed or orientation, could also have the effect of creating a cutoff in the emission since the observed flux from the jet follows $F_\nu \propto \delta^{3+\alpha_r}$. Millimeter-wave VLBI observations are important to study this transition region.

The lower redshift objects appear to have distinct X-ray properties. For example, both 3C 111 and 3C 120 have very steep X-ray spectra ($\alpha_x > 2$) and the X-rays could have a thermal origin (Dermer & Schlickeiser 1993; Grandi et al. 1997). This steep soft X-ray spectral component would lie at frequencies below the *ROSAT* PSPC response at the higher redshifts of the quasars in the sample. Indeed, at higher X-ray energies, both radio galaxies have flatter spectra, similar to those of quasars (Petre et al. 1984). Leach, McHardy, & Papadakis (1995) have shown that the spectral slope of the low-redshift quasar 3C 273 is -2.7 in the low-energy band (0.1–0.3 keV) of the *ROSAT* PSPC and -0.5 in the hard band (1.5–2.4 keV). Also, as discussed earlier, 0736+017, at a redshift of 0.19, has an X-ray spectral index $\gtrsim 2$ if photoelectric absorption by Galactic molecular gas is taken into account.

Three sources, 0836+710, NRAO 140, and 4C 39.25, clearly show radio to millimeter variability that is directly proportional the X-ray variability. As discussed by Marscher (1988), this would occur if the quantity $N_0 x$ is nearly constant with time, with N_0 varying inversely as the line of sight distance through the source x . However, an increase in the Doppler factor would also have a similar signature (see Marscher, Gear, & Travis 1992 and below). It is further likely, from the general considerations of Bloom & Marscher (1996) and the SSC calculations in § 3, that the high states of radio to X-ray (and in some cases γ -ray) emission are associated with higher high-energy cutoffs to the electron distribution. This increases the X-ray flux density by another factor of $2 \ln \gamma_{\max}$. This would predict that if the

γ -rays are from first-order SSC, then the X-ray flux density should increase by a slightly larger factor than the synchrotron flux density. In cases for which the entire spectrum increases by a fixed amount, the increase can be attributed to a change in the Doppler factor.

Models that involve the scattering of external radiation from the relativistic electrons in jets (see, e.g., Melia & Königl 1989; Dermer & Schlickeiser 1993) would also explain this linear relation between millimeter and X-ray flux if changes in N_0 were solely responsible for the variations in the synchrotron and scattered fluxes. This would be the case if density fluctuations occurred while the magnetic field remained constant (see Bloom & Marscher 1996).

Of the six sources in our sample that were detected in high-energy γ -rays, two were in a higher state at millimeter or centimeter wavelengths at the time of the detection. The source 0836+710 showed a factor of 2 increase in the millimeter and X-ray flux densities when it was detected in γ -rays relative to earlier times. Though 0804+499 was only observed at millimeter wavelengths several months before and after the γ -ray detection, centimeter-wave flux densities clearly increased by a factor of 3 between 1991 August and 1992 December. The other sources (0917+449, 0954+556, 1611+343, and 1633+382) were not well observed during the time of the EGRET observations.

The physical relationships among the various parameters are often complicated and hidden by selection effects. We have used statistical tests to attempt to reveal underlying relationships. We find that the X-ray luminosity is correlated with the radio core and millimeter-wave luminosities. However, the strong correlation is probably due in part to luminosity-redshift bias.

There are many aspects of this work that should be continued to gain a better understanding of the relationship between the radio to IR and X-ray to γ -ray properties of FRSQs. Because many sources in this sample exhibit spectral turnovers near 40 GHz, and these turnovers indicate that the emission originates from the innermost region of the jet, they should be observed with VLBI at 43 GHz (VLBA) and in the 1–3 mm range (various arrays) to try to resolve these inner regions and gain a better understanding of the physical conditions at the base of the radio jet. In addition, the angular sizes derived from these VLBI images can be used for more accurate Compton calculations in conjunction with X-ray and γ -ray observations. Simultaneous multiwaveband and VLBI observations would relate the variations at different frequencies both to each other and to changes in the structure of the jet. Time-dependent models of SSC emission from relativistic jets should be developed to replace the crude uniform spherical source approximation used in this study. Finally, complete samples chosen using various well-defined criteria should be studied thoroughly to establish statistical relationships as well as to elucidate the effects of those selection criteria. Together, future studies such as these should lead to a more complete understanding of the nature of the nonthermal emission in FRSQs.

We thank the anonymous referee for many useful comments and patience while the final manuscript was being revised. The authors gratefully acknowledge the use of data from the service observing programs at both the JCMT and UKIRT and thank the staffs of these telescopes for carrying out the observations on our behalf. The JCMT is operated

jointly by the UK Particle Physics and Astronomy Research Council, the Netherlands Organization for the Advancement of Pure Research (ZWO), the Canadian National Research Council (NRC), and the University of Hawaii. UKIRT is operated by the Royal Observatory, Edinburgh on behalf of the UK Particle Physics and Astronomy Research Council. The National Radio Astronomy Observatory is operated by Associated Universities, Inc., under cooperative agreement with the US

National Science Foundation. This material is based upon work supported by the NSF under grants AST 91-16525 (Boston University) and AST 91-20224 (University of Michigan), and by NASA under grants NAG 5-1566, NAG 5-1943 (Boston University). S. Bloom also gratefully acknowledges a grant by the Israel Council for Higher Education during his stay at Technion (Israel Institute of Technology) and an NRC Research Fellowship while at NASA/GSFC.

REFERENCES

- Band, D. L., & Grindlay, J. E. 1986, *ApJ*, 308, 576
 Bania, T. M., Marscher, A. P., & Barvainis, R. 1991, *AJ*, 101, 2147
 Bevington, P. R. 1969, *Data Reduction and Error Analysis for the Physical Sciences* (New York: McGraw-Hill)
 Biretta, J. A., et al. 1986, *ApJ*, 308, 93
 Bloom, S. D. 1994, Ph. D. thesis, Boston Univ.
 Bloom, S. D., & Marscher, A. P. 1991, *ApJ*, 366, 16
 ———. 1996, *ApJ*, 461, 457
 Bloom, S. D., Marscher, A. P., Gear, W. K., Aller, H., Aller, M., & Teräsraanta, H. 1994, *AJ*, 108, 398
 Brown, L. M. J., et al. 1989, *ApJ*, 340, 149.
 Browne, I. W. A., & Murphy, D. W. 1987, *MNRAS*, 226, 601
 Brunner, H., Lamer, G., Worrall, D. M., & Staubert, R. 1994, *A&A*, 287, 436
 Cohen, M. H., et al. 1975, *ApJ*, 201, 249
 Comastri, A., et al. 1997, *ApJ*, 480, 534
 Dermer, C. D. 1993, in *Compton Gamma-Ray Observatory*, ed. M. Friedlander, N. Gehrels, & D. Macomb (New York: AIP), 541
 Dermer, C. D., & Schlickeiser, R. 1993, *ApJ*, 416, 458
 Eckart, A., et al. 1986, *A&A*, 168, 17
 ———. 1987, *A&AS*, 67, 121
 Elvis, M., Lockman, F. J., & Wilkes, B. J. 1989, *AJ*, 97, 777
 Fichtel, C. E., et al. 1994, *ApJS*, 94, 551
 Frail, D. A., Weisberg, J. M., Cordes, J. M., & Mathers, C. 1994, *ApJ*, 436, 144
 Gear, W. K., et al. 1994, *MNRAS*, 267, 167
 Ghissellini, G., Maraschi, L., & Treves, A. 1985, *A&A*, 146, 204
 Grandi, P., et al. 1997, *ApJ*, 487, 636
 Hartman, R. C., et al. 1992, in *The Compton Observatory Science Workshop*, ed. C. R. Shrader, N. Gehrels, & B. Dennis (NASA Conf. Publ. 3137), 116
 Isobe, T., & Feigelson, E. D. 1990, *BAAS*, 22, 917
 Isobe, T., Feigelson, E. D., & Nelson, P. I. 1986, *ApJ*, 306, 490
 Jones, T. W., O'Dell, S. L., & Stein, W. A. 1974a, *ApJ*, 188, 353
 ———. 1974b, *ApJ*, 192, 261
 Kembhavi, A., Feigelson, E. D., & Singh, K. P. 1986, *MNRAS*, 220, 51
 Königl, A. 1981, *ApJ*, 243, 700
 Krichbaum, T. P., et al. 1990, *A&A*, 230, 271
 Ku, W. H.-M., Helfand, D. J., & Lucy, L. B. 1980, *Nature*, 288, 323
 Leach, C. M., McHardy, I. M., & Papadakis, I. E. 1995, *MNRAS*, 272, 221
 Ledden, J. E., & O'Dell, S. L. 1985, *ApJ*, 298, 630
 Liszt, H. S., & Wilson, R. W. 1993, *ApJ*, 403, 663
 Malaguti, G., Bassani, L., & Caroli, E. 1994, *ApJS*, 94, 517
 Marscher, A. P. 1977, *ApJ*, 216, 244
 ———. 1980, *ApJ*, 235, 386
 ———. 1987, in *Superluminal Radio Sources*, ed. J. A. Zensus & T. J. Pearson (Cambridge: Cambridge Univ. Press), 280
 ———. 1988, *ApJ*, 334, 552
 Marscher, A. P., & Gear, W. K. 1985, *ApJ*, 298, 114
 Marscher, A. P., Gear, W. K., & Travis, J. P. 1992, in *Variability of Blazars*, ed. E. Valtaoja & M. Valtonen (Cambridge: Cambridge Univ. Press), 85
 Marscher, A. P., Zhang, Y. F., Shaffer, D. B., Aller, H. D., & Aller, M. F. 1991, *ApJ*, 371, 491
 Mattox, J. R., et al. 1993, *ApJ*, 410, 609
 ———. 1996, *ApJ*, 461, 396
 Melia, F., & Königl, A. 1989, *ApJ*, 340, 162
 Owen, F. N., Helfand, D. J., & Spangler, S. R. 1981, *ApJ*, 250, L55
 Padovani, P. 1992, *A&A*, 256, 399
 Pearson, T. J., & Readhead, A. C. S. 1984, *ARA&A*, 22, 97
 ———. 1988, *ApJ*, 328, 114
 Petre, R., Mushotzky, R. F., Krolik, J. H., & Holt, S. S. 1984, *ApJ*, 280, 499
 Sambruna, R. 1997, *ApJ*, 487, 536
 Schwab, F. R., & Cotton, W. D. 1983, *AJ*, 88, 688
 Stark, A. A., et al. 1992, *ApJS*, 79, 77
 Steppe, H., et al. 1988, *A&AS*, 75, 317
 Tananbaum, H., et al. 1979, *ApJ*, 234, L9
 Thompson, D. J., et al. 1993, *ApJ*, 415, L13
 ———. 1995, *ApJS*, 101, 259
 ———. 1996, *ApJS*, 107, 227
 Tornikoski, M., et al. 1994, *A&A*, 289, 673
 Unwin, S. C., et al. 1994, *ApJ*, 432, 103
 ———. 1997, *ApJ*, 480, 596
 von Linde, J., et al. 1993, *A&A*, 267, L23
 Wehrle, A. E., & Mattox, J. R. 1994, in *AIP Conf. Proc. 304, The Second Compton Symposium*, ed. C. E. Fichtel, N. Gehrels, & J. P. Norris (New York: AIP), 688
 Wilkes, B. J. 1992, *ROSAT-PROS Users Guide* (Cambridge, MA: Smithsonian Astrophys. Obs.)
 Wilkes, B. J., & Elvis, M. 1987, *ApJ*, 323, 243
 Worrall, D. M., Giommi, P., Tananbaum, H., & Zamorani, G. 1987, *ApJ*, 313, 596
 Worrall, D. M., & Wilkes, B. J. 1990, *ApJ*, 360, 396
 Zamorani, G., et al. 1981, *ApJ*, 245, 357
 Zhang, Y. F., & Marscher, A. P. 1994, in *Proc. of the 1993 ROSAT Science Symposium*, ed. E. Schlegel & R. Petre (New York: AIP), 406
 Zhou, Y. Y., et al. 1997, *ApJ*, 484, L47